About the Journal | Preparing Your Manuscript | Index-Term Keywords | Contact Editorial Office

Detailed Status Information

Manuscript #	POF25-AR-17659
Current Revision #	0
Other Version	POF25-AR-17659R
Submission Date	07-Oct-2025 06:13:59 **Days Since Original Submission: 62**
Revision Due Date	06-Dec-2025
Current Stage	Revised Manuscript Received from Author **Days in Folder: 11**
Title	ROSSBY WAVE RADIATION ON THE B-PLANE BY WESTERN AND EASTERN BOUNDARY CURRENTS
Manuscript Type	Article
Permissions	No, no figures/tables have been previously published.
Special Topic	N/A
Subject Area	Geophysical Flows
Topical Keywords	vortex flows : vortex dynamics, waves / free surface flows :, geophysical and geological flows :
Authors	1 Dr. Vladimir Grigorievich Gnevyshev (P P Shirshov Institute of Oceanology RAS)
	2 Dr. Vladimir Travkin (Saint Petersburg State University Institute of Earth Sciences) (corr-auth)
	3 Dr. Tatyana Belonenko (Saint Petersburg State University Institute of Earth Sciences)

Abstract	The linear problem of Rossby wave radiation by meridional boundary currents is considered. The spectral problem is conditionally divided into two regions: the long-wavelength region ($l < 0.5$) and the short-wavelength region ($l > 0.5$) (where l is the meridional wavenumber normalized to the current width). It is shown that in the long-wavelength part of the spectrum, a quasimonochromatic Rossby wave is radiated into the open ocean, and an asymmetry between the western and eastern boundary currents is observed. The western boundary current radiates Rossby waves with small growth increments. The wavenumber and group velocity of the radiated Rossby wave in the open ocean are practically zonal and oppositely directed. The eastern current, conversely, radiates Rossby waves with large growth increments. The wavenumber is directed almost meridionally; the group velocity is directed westward. Rossby waves radiated by the eastern current are an order of magnitude longer than waves radiated by the western current. In the short-wavelength region, the radiation of Rossby waves into the open ocean disappears. The asymmetry between east and west also disappears. The solution, for both the eastern and western boundary currents, converges to a varicose Rayleigh mode and consists of a chain of small (compared to the current width) cyclones and anticyclones located on the outer boundary of the current (on the open ocean side). Verification of this model using the example of the Lofoten Basin in the Norwegian Sea has shown that typical nondimensional β values are closer to 0.01 rather than β = 0.5.

Associate Editor	Assigned
Author Referee Suggestions to Include	Victor Shrira (Keele University School of Computing and Mathematics), Eugene Morozov (Shirshov Institute of Oceanology, Russian Academy of Sciences), Sergei Badulin (P P Shirshov Institute of Oceanology RAS), Maxim Budyansky, Eugene Benilov (University of Limerick Department of Mathematics and Statistics), Georgi Sutyrin (URI Graduate School of Oceanography), Alexander Shchepetkin (University of Limerick Department of Mathematics and Statistics), Eugenyi Zakharchuk (Saint Petersburg State University Institute of Earth Sciences)
Author Referee Suggestions to Exclude	N/A
Applicable Funding Sources	Saint Petersburg State University (SPbU) ✔ : 129659573 Russian Science Foundation (RSF) ✔ : 25-17-00021 Minobrnauka | Ministry of Science and Higher Education of the Russian Federation (Minobrnauki of Russia) ✔ : FMWE-2024-0017
Data Availability Statement	The data that support the findings of this study are available from the corresponding author upon reasonable request. View Data Availability Statement Response
Invited Submission	No
Resubmission of Manuscript	No
English Language Editing	Has your manuscript been edited by an English language editing service? No
Ethics Approval	No experiments on animal or human subjects were used for the preparation of the submitted manuscript.
Electronic Forms	1 of 1 forms complete - Vladimir Travkin (Corr): completed on 27-Nov-2025 (AIPP Standard LTP Form)
Candidate for Cover	

1

Stage	Start Date
Revised Manuscript Received from Author	27-Nov-2025 04:30:49
Waiting for Revised Manuscript from Author	15-Nov-2025 22:39:26
Decision Sent to Author	15-Nov-2025 22:39:25
Decision Letter Being Prepared	15-Nov-2025 10:25:27
Editor Decision Completed	15-Nov-2025 10:25:27
Associate Editor Decision Completed	15-Nov-2025 10:25:26
Securing Reviewer(s)	15-Nov-2025 10:24:20
Associate Editor Decision Started	15-Nov-2025 10:24:06
All Reviews Received	15-Nov-2025 10:24:06
Securing Reviewer(s)	15-Nov-2025 10:24:05
Associate Editor Decision Started	15-Nov-2025 10:24:05
All Reviews Received	15-Nov-2025 10:24:05
All Reviewers Secured	15-Nov-2025 10:24:05
Review Received	03-Nov-2025 15:05:34
All Reviewers Secured	30-Oct-2025 04:07:14
Review Started	30-Oct-2025 04:07:14
Securing Reviewer(s)	29-Oct-2025 18:04:32
Review Started	29-Oct-2025 13:30:12
Securing Reviewer(s)	27-Oct-2025 14:27:00
Review Started	27-Oct-2025 11:29:58
Securing Reviewer(s)	18-Oct-2025 20:10:28
Review Started	16-Oct-2025 17:09:23
Securing Reviewer(s)	14-Oct-2025 03:53:32
Manuscript File Deleted	13-Oct-2025 17:17:29
Manuscript File Added	13-Oct-2025 17:15:50
Securing Reviewer(s)	13-Oct-2025 15:10:39
Review Started	13-Oct-2025 10:38:39
First Reviewer Secured	13-Oct-2025 10:38:39
Securing Reviewer(s)	08-Oct-2025 11:43:07
Associate Editor Assigned	08-Oct-2025 08:03:02
Editor Assigned	08-Oct-2025 08:03:02
Manuscript Submitted to Journal Office	08-Oct-2025 08:03:02
Submission Check by Journal Office Completed	08-Oct-2025 08:03:02
Submission Check by Journal Office Started	08-Oct-2025 05:52:20
Editor Assigned	08-Oct-2025 05:52:20
Manuscript Submitted to Journal Office	08-Oct-2025 05:52:19
Awaiting Author Adjustment/Approval of Converted Files	07-Oct-2025 11:42:13
Submission Check by Journal Office Failed	07-Oct-2025 11:42:13
Submission Check by Journal Office Started	07-Oct-2025 09:43:23
Editor Assigned	07-Oct-2025 09:43:23

ROSSBY WAVE RADIATION ON THE B-PLANE BY WESTERN AND EASTERN BOUNDARY CURRENTS

V. G. Gnevyshev[a,b], V. S. Travkin[a,c,d], T. V. Belonenko[a*]

[a] St. Petersburg University, St. Petersburg, 199034 Russia

[b] Shirshov Institute of Oceanology, Russian Academy of Sciences, Moscow, 117997 Russia

[c] Peter the Great St. Petersburg Polytechnic University, St Petersburg, 195251 Russia

[d] N.N. Zubov's State Oceanographic Institute, Roshydromet, Moscow, 119034, Russia

[*]e-mail: vtravkin99@gmail.com

Abstract

The linear problem of Rossby wave radiation by meridional boundary currents is considered. The spectral problem is conditionally divided into two regions: the long-wavelength region ($l < 0.5$) and the short-wavelength region ($l > 0.5$) (where l is the meridional wavenumber normalized to the current width). It is shown that in the long-wavelength part of the spectrum ($l < 0.5$), a quasimonochromatic Rossby wave is radiated into the open ocean, and an asymmetry between the western and eastern boundary currents is observed. The western boundary current radiates Rossby waves with small growth increments. The wavenumber and group velocity of the radiated Rossby wave in the open ocean are practically zonal and oppositely directed (the phase propagates westward, the group velocity is directed eastward). The eastern current, conversely, radiates Rossby waves with large growth increments. The wavenumber is directed almost meridionally, and the group velocity is directed westward. Rossby waves radiated by the eastern current are an order of magnitude longer than waves radiated by the western current. In the short-wavelength region ($l > 0.5$), the radiation of Rossby waves into the open ocean disappears. The asymmetry between east and west also disappears. The solution, for both the eastern and western boundary currents, converges to a varicose Rayleigh mode and consists of a chain of small (compared to the current width) cyclones and anticyclones located on the outer boundary of the current (on the open ocean side). Verification of this model using the example of the Lofoten Basin in the Norwegian Sea has shown that typical nondimensional β values at mid-latitudes are closer to 0.01 rather than β = 0.5.

Keywords: nonzonal current, Rossby waves, western and eastern boundary currents, β-destabilizing effect

1. Introduction

Earth's rotation profoundly shapes large-scale ocean circulation, driving complex, nonlinear interactions among currents, Rossby and Kelvin waves, mesoscale eddies, and tides (Salmon, 1998; Huang, 2010; Klinger and Haine, 2019). Seafloor topography, including ridges and trenches, both generates and guides/dissipates internal wave energy (Gnevyshev et al., 2021a, 2022, 2023; Pedlosky, 1987).

These effects are particularly significant in mesoscale ocean circulation, where horizontal scales exceed the baroclinic Rossby deformation radius. Mesoscale eddies are crucial energy carriers, often contributing over 40% (and sometimes >70%) of total mesoscale kinetic energy (Travkin and Belonenko, 2021; Chelton et al., 2011). They drive energy transfer from mesoscale to submesoscale via filament stretching, essential for energy cascades and inter-scale interactions (Arbic et al., 2012; Zhmur et al., 2022, 2023a,b,c).

Large-scale circulation is fundamentally governed by barotropic potential vorticity conservation (Pedlosky, 1987; Zhmur, et al 2021), dictating cyclonic circulation over topographic slopes in the Northern Hemisphere. However, at mesoscale, bottom topography often exerts a stronger influence than the β-effect (Gnevyshev et al., 2021a, 2022).

Baroclinic instability of jet-like lateral currents, especially near strong permanent currents, is a key research focus (LaCasce et al., 2000, 2024; Chelton et al., 2011). Ocean's potential energy can vastly exceed kinetic energy (Gill et al., 1974; Ferrari and Wunsch, 2009; Smith, 2007), with baroclinic instability converting this into eddy kinetic energy (Lorenz, 1955). This process is most prominent along continental slopes, generating numerous mesoscale eddies (Zatsepin and Elkin, 2024; Charney, 1990; Eady, 1949; Pedlosky, 1987). Steeper slopes enhance eddy generation (Bower et al., 2002, 2009; Isachsen, 2011; Trodahl and Isachsen, 2018). Bottom topography controls boundary current pathways and eddy/wave trajectories, often following isobaths (Belonenko et al., 2021, 2018; Sandalyuk et al., 2021; Gnevyshev et al., 2021a, 2022c). Mesoscale eddies frequently form at current peripheries (Travkin et al., 2024; Belonenko et al., 2024).

While classical theory (Huang, 2010; Klinger and Haine, 2019) constrains the growth of eddy energy under weak zonal shear, the presence of a meridional current component fundamentally changes this picture. The addition of a meridional flow can significantly intensify baroclinic instability, generating eddies whose kinetic energy exceeds that of the mean current (Robinson and McWilliams, 1974; Rhines, 1977; Spall, 2000). This underscores the essential role of the background circulation in both producing and amplifying mesoscale structures, which subsequently radiate Rossby waves—key agents in feedbacks across oceanic scales. Therefore, background flows containing a meridional component not only enhance baroclinic instability but also fundamentally reorganize energy pathways, strongly influencing the generation and radiation of Rossby waves and shaping large-scale ocean circulation.

Early ideas posited open-ocean eddies originate from radiation by jet-like western boundary currents (Hogg and Johns, 1995). For eastern boundary currents, localized buoyancy sources, nonlinear waves, and the β-plume mechanism proved fruitful. Subsequent studies found such radiative processes also stem from flow non-zonality (Fantini and Tung, 1987; Hristova et al., 2008; Berloff and Kamenkovich, 2013a,b; Afanasyev et al., 2012), with eastern boundary currents often being more unstable.

A zonal current of the hat-profile type cannot radiate Rossby waves into the open ocean. Kamenkovich and Pedlosky (1996, 1998a,b) showed that the meridional tilt of jets decisively

influences perturbation spectra and radiation ability. Radiating instabilities – modes propagating beyond their generation region – require non-zonal currents. Strictly zonal flows trap unstable modes, preventing far-field energy transfer. Non-zonal currents, with a meridional component, yield wave-like solutions that effectively radiate perturbations over vast distances. Thus, a meridional component fundamentally reorganizes wave energy transport, forming "leaky" or radiating modes. Western and eastern boundary currents are active sources of large-scale wave radiation, influencing distant regions (Gnevyshev et al., 2021a, 2023). These studies are crucial for understanding ocean energy transfer. Analysis of characteristic spatial scales of radiation is key, with theoretical estimates showing decay lengths of hundreds of kilometers, raising questions about local mesoscale disturbances' influence on regional and global circulation. Satellite altimetry confirms correlations between eddy activity in strong currents (e.g., Gulf Stream, Kuroshio) and remote low-frequency variability (Belonenko and Kubryakov, 2014; Belonenko et al., 2016, 2018, 2023; Gnevyshev et al., 2019, 2020, 2021b, 2022a,b).

One hypothesis attributes open-ocean mesoscale eddies to Rossby wave radiation from western boundary currents (Fantini and Tung, 1987; Kamenkovich and Pedlosky, 1996). However, historical studies (Talley, 1983, 2011; Howard and Drazin, 1964) on strictly zonal currents showed localized instabilities with no effective far-field energy radiation. Gnevyshev et al. (2025) recently confirmed strictly zonal flows do not radiate Rossby waves. This establishes flow non-zonality (e.g., meridional jet tilt or topography interaction) as a necessary condition for radiating waves. The hypothesis of mesoscale eddy generation by boundary current radiation thus requires revision: only asymmetric, non-zonal western boundary currents excite radiating modes propagating into the ocean interior. Radiation efficiency depends on jet curvature, flow structure, and background planetary vorticity gradients.

The nonlinear stage of radiating instabilities is critical (Davey and Killworth, 1989; Kamenkovich and Pedlosky, 1998a,b). Numerical modeling reveals a qualitative shift from quasi-linear wave propagation to coherent vortex structures capable of long-range transport at sufficient initial disturbance amplitudes (Gnevyshev et al., 2025). This resembles soliton formation, requiring specialized mathematical tools. Fantini and Tung (1987) identified weakly unstable modes radiating energy. Hristova et al. (2008) generalized radiative instability to both western and eastern boundary currents, finding additional modes for $\beta = 0.5$ (absent in Fantini and Tung (1987) for $\beta = 0.01$) (Supplementary Figs. S1, S3, S4). Eastern boundary modes exhibited greater zonal extent. Wang et al. (2012, 2013) further developed the idea of generating oceanic striations via radiative instabilities. However, earlier studies (Hristova et al., 2008; Fantini and Tung, 1987) were limited by one-dimensional perturbation sections, failing to capture the two-dimensional nature of radiation. Thus, advancing radiative instability theory requires accounting for two-dimensional spatial structure and verifying previous results. Analyzing asymmetry between eastern and western boundary currents in generating radiating modes is particularly important. This study extends research on boundary current instabilities, refining previous solutions and their qualitative description. We independently verified numerical solutions from Fantini and Tung (1987) and Hristova et al. (2008), confirming additional unstable roots. Unlike most previous studies, we construct full two-dimensional fields – both meridional displacement and velocity components – for weakly unstable radiating solutions, revealing subtle spatial features beyond the jet.

Analysis of two-dimensional velocity fields shows that, in the long-wave limit, weakly unstable solutions represent transverse-shear flows. A fundamental asymmetry exists: eastern current perturbations exhibit greater longitudinal extent and anisotropy (directed radiation), while western currents show more localized modes with significantly less energy transmitted into the open ocean. These differences underscore background flow geometry's importance. For the eastern

boundary current, radiating modes have pronounced zonal elongation. The western boundary current shows shear modes primarily meridionally oriented, indicating limited effective radiation.

As the spectrum shifts to shorter waves, anisotropy weakens. Wave modes lose elongation, becoming localized, mesoscale-eddy-like structures near the jet boundary (Capet et al., 2008; Gnevyshev & Belonenko, 2025). This transforms the instability mechanism: radiating modes dominate in the long-wave limit, while localized vortex modes (tens of kilometers) prevail in the short-wave range. With increasing longitudinal wavenumber, solutions for both western and eastern boundary currents transform into a Rayleigh varicose mode, asymptotically approaching Helmholtz instability.

The aim of this paper is to deepen the understanding of Rossby wave radiation mechanisms by non-zonal boundary currents (western and eastern) on a β-plane.

This paper is organized as follows. Section 2, "Problem Statement. Meridional Rectangular Flow on a β-Plane," presents the fundamental problem statement. Section 3, "Boundary-value problem in the plane-wave basis," details the formulation of the boundary-value problem, including basic equations (3a), boundary conditions (3b), and matching of solutions (3c). In Section 4, "Western Meridional Boundary Current," we analyze its dynamics, presenting its dispersion relation (4a), analytical asymptotics (4b), and analytical expression for zonal displacement and velocity field (4c). A parallel analysis for the eastern meridional boundary current is in Section 5, "Eastern Meridional Boundary Current." Section 6, "Numerical Solutions," describes the numerical methods. In Section 7, "Interpretation of the theoretical model for the Lofoten Basin," we apply results to interpret dynamics of the Lofoten Basin, justifying our choice. Finally, Section 8, "Conclusions and Discussion," summarizes findings, discusses implications, and suggests future research.

2. Problem Statement. Meridional Rectangular Flow on a β-Plane

We then begin with the linearized vorticity equation for the stream function

$\Psi = \Phi(x) \exp i l (y - ct)$, where l is the meridional component of the wave number, c is the meridional component of the phase speed, in the form (Fantini and Tung, 1987).

For definiteness, we assume that the background meridional velocity ($V > 0$), since negative velocities can be obtained by mirror reflection with respect to the zonal direction $c = \omega/l$ – meridional component of the phase speed; the x-axis is directed eastward, the y-axis – northward; t – time. Then we obtain

$$\Phi_{xx} + \frac{i\beta}{l(c-V)}\Phi_x - \left(l^2 - \frac{V_{xx}}{c-V}\right)\Phi = 0. \tag{1}$$

In this case $V = $ const, each wavenumber satisfies the dispersion relation

$$\omega = -\frac{\beta k}{k^2 + l^2} + lV, \tag{2}$$

where k is the zonal component of the wave number and V is the meridional stationary flow.

The matching conditions for the piecewise-constant velocity profile are identical to those used in Fantini and Tung (1987), Kamenkovich and Pedlosky (1996), and Hristova et al. (2008), and take the form:

$$\Delta\left[\frac{\Phi}{c-V}\right]=0, \tag{3}$$

$$\Delta\left[\Phi_x(c-V)+ib\,\Phi\right]=0, \quad b\equiv\frac{\beta}{l}, \tag{4}$$

where $\Delta[...]$ indicates the jump that the quantity in brackets experiences across the interface. Equation (3) represents the continuity of the normal component of velocity (or displacement), or the continuity of mass transport in the direction normal to the interface (in the meridional direction).

2.1. Meridional flow with a rectangular profile (hat-shaped)

Consider the profile V of a hat-shaped flow (see Fig. 1); the half-width of the flow is d:

$$\begin{aligned}
V &= 0, \quad x > d,\\
V &= V_0, \quad -d \le x \le d,\\
V &= 0, \quad x < -d.
\end{aligned} \tag{5}$$

We choose the jet half-width, d, as the length scale. Wavenumbers are then non-dimensionalized $k^* = k\,d$, $l^* = l\,d$, spatial coordinates $x^* = x/d$, $y^* = y/d$, and the phase velocity $c^* = c/V_0$. A nondimensional parameter $\beta^* = \beta\,d^2/V_0$ then appears in the problem (hereafter, the asterisks are omitted).

3. Boundary-value problem in the plane-wave basis

a. Basic equations

The flow is defined as:

$$\begin{aligned}
V &= 0, \quad x > 1,\\
V &= 1, \quad -1 \le x \le 1,\\
V &= 0, \quad x < -1.
\end{aligned} \tag{6}$$

We seek a solution in the form of:

$$\begin{aligned}
\Phi_1 &= T\exp(i\,k_2 x), \quad x \ge 1,\\
\Phi_2 &= A\exp(i\,k_{11}x)+B\exp(i\,k_{12}x), \quad -1 \le x \le 1,\\
\Phi_3 &= P\exp(i\,k_3 x), \quad x \le -1.
\end{aligned} \tag{7}$$

Here, T, A, B, and P are constants.

The dispersion relation (2) can be rewritten in the following form:

$$k_{11,12} = \frac{1}{2(c-1)} \left\{ -b \pm \left[b^2 - 4(1-c)^2 l^2 \right]^{1/2} \right\},$$

$$k_{3,2} = \frac{1}{2c} \left\{ -b \pm \left[b^2 - 4c^2 l^2 \right]^{1/2} \right\}, \quad \mathrm{Im}(k_3) \le 0; \quad \mathrm{Im}(k_2) \ge 0. \tag{8}$$

b. Boundary conditions

In the earliest studies on Rossby wave instability over a current, the boundary condition at infinity was taken as a decay condition (Howard and Drazin, 1964) if the wavenumbers were complex. If the wavenumbers are real (waves of neutral stability), then a radiation condition is imposed—the transverse component of the group velocity is directed toward the open ocean. In this problem, the transverse component corresponds to the zonal direction. In later studies, the concept of group velocity was also formulated for weakly unstable solutions (Talley, 1983; Hristova et al., 2008; Kamenkovich and Pedlosky, 1996; Kamenkovich, 2013).

Since the discriminant in Equation (8) is preceded by a plus-minus sign, we can always select the appropriate sign for the imaginary part of the wavenumber to satisfy the decay condition at infinity for both western and eastern boundary currents.

If equation (2) is rewritten as a quadratic equation in k, i.e., $k^2 + b/(c-1) + l^2 = 0$, then the product of the wavenumbers $k_{11,12}$ equals l^2 (by Vieta's theorem) and is always real. A similar statement holds for $k_{3,2}$; therefore, the wavenumbers k_3 and k_2 have opposite imaginary parts, and we can always choose a wavenumber that ensures decay at infinity. However, in the works of Wang et al. (2019), we read: "Note that the roots of k are always a pair of complex conjugates for all eigenmodes since the product of the two roots is l^2, which is real." As we will show later, this statement is not correct. The eigenvalues only asymptotically approach complex conjugacy when $l \gg 1$, but they are never truly complex conjugates for any finite l (see Supplementary Figs. S2, S5).

In the work of Fantini and Tung (1987), in our view, the generalization of the group velocity to any unstable waves — not necessarily weakly unstable solutions—was unjustified. The authors postulate the following formulas for the group velocity (see Fantini and Tung, 1987):

$$k(\omega_r + i\omega_i) = k\,\omega_r + i\,\omega_i \frac{d\,k}{d\,\omega_r} = k_r + i\frac{\omega_i}{c_{gx}}; \quad c_{gx} = \mathrm{Re}\left[\frac{\beta(k^2 - l^2)}{(k^2 + l^2)^2} \right]. \tag{9}$$

The authors consider the zonal group velocity for any complex wave vectors (see Fantini and Tung, 1987, caption to Figure 3 in this paper). The relation $(k = k_r + i k_i, \quad k_r \gg k_i)$ is not required for them. We believe that such a generalization is incorrect.

We believe that the correct generalization applies only to weakly unstable solutions. Under the condition $(k_r \gg k_i)$ and assuming solution smoothness, such a generalization is permissible (Bühler, 2009):

$$k(\omega_r + i\omega_i) = k(\omega_r) + i\,\omega_i \frac{d\,k}{d\,\omega_r} = k_r + i\frac{\omega_i}{c_{gx}}, \tag{10}$$

8

$$\psi = \exp\left[\omega_i\left(t - x/c_{gx}\right)\right]\exp\left[i\left(k_r x + ly - \omega_r t\right)\right], \tag{11}$$

from which it follows that perturbations propagate to the right for positive group velocity c_{gx} and to the left for negative.

c. Matching of solutions

The matching at $x = 1$ takes the form

$$T = \frac{c\exp(-ik_2)}{c-1}\left[A\exp(ik_{12}) + B\exp(ik_{11})\right], \tag{12}$$

$$A\left[(c-1)^2 k_{12} - c^2 k_2 - b\right]\exp(ik_{12}) + B\left[(c-1)^2 k_{11} - c^2 k_2 - b\right]\exp(ik_{11}) = 0. \tag{13}$$

The matching at $x = -1$ takes the form

$$P = \frac{c\exp(ik_3)}{c-1}\left[A\exp(-ik_{12}) + B\exp(-ik_{11})\right], \tag{14}$$

$$A\left[(c-1)^2 k_{12} - c^2 k_3 - b\right]\exp(-ik_{12}) + B\left[(c-1)^2 k_{11} - c^2 k_3 - b\right]\exp(-ik_{11}) = 0. \tag{15}$$

The determinant of the matrix – the dispersion relation (13), (15) – takes the form:

$$\begin{aligned}
&\left[(c-1)^2 k_{12} - c^2 k_2 - b\right]\left[(c-1)^2 k_{11} - c^2 k_3 - b\right]\exp\left(i[k_{12} - k_{11}]\right) = \\
&= \left[(c-1)^2 k_{11} - c^2 k_2 - b\right]\left[(c-1)^2 k_{12} - c^2 k_3 - b\right]\exp\left(-i[k_{12} - k_{11}]\right)
\end{aligned} \tag{16}$$

Equation (16) is a special case of the equation from (Kamenkovich and Pedlosky, 1996, equation 16), written in a different coordinate system. In (Kamenkovich and Pedlosky, 1996), the x-axis is directed north and the y-axis west, perpendicular to the flow.

4. Western meridional boundary current

a. Dispersion relation

This study considers three configurations: the meridional jet, the western boundary current, and the eastern boundary current. We adopt the following notations for velocities: c_w – for the western boundary current, c_e – for the eastern boundary current.

We take the right half of the solution for the jet and, instead of the left boundary condition (at $x = -1$), impose a rigid wall at the center, from which we obtain $B = -A$. Then the solution for the western boundary current takes the form:

$$\begin{aligned}
&\Phi_1 = c_w\left\{\exp\left[ik_2(x-1)\right]\right\}\left[\exp(ik_{12}) - \exp(ik_{11})\right], \quad x \geq 1, \quad \mathrm{Im}(k_2) \geq 0, \\
&\Phi_2 = (c_w - 1)\left[\exp(ik_{12}x) - \exp(ik_{11}x)\right], \quad 0 \leq x \leq 1
\end{aligned} \tag{17}$$

The right boundary condition (13) at $x = 1$ remains unchanged. The dispersion relation takes the form:

$$\left[(c_w-1)^2 k_{12} - c_w^2 k_2 - b\right]\exp(ik_{12}) = \left[(c_w-1)^2 k_{11} - c_w^2 k_2 - b\right]\exp(ik_{11}). \tag{18}$$

This result was obtained by Fantini and Tung (1987).

b. Analytical asymptotics of the dispersion relation

This section discusses the construction of the asymptotics of the dispersion relation (18) for $\beta \to 0, \quad l > 0$.

For $b \to 0$, the wavenumbers (8), for any finite behavior of the eigenvalue c, approach the asymptotic $k_{3,2} \to \mp i\, l$. In the open ocean, there is no radiation, i.e., no oscillations of the eigenfunction. The behavior of the second pair of wavenumbers $k_{11,12}$ exhibits a branching point in the analysis. Let us consider two cases.

1. If $(c-1)^2 l^2$ does not tend to zero, since $l \to \infty$, this means that c does not approach unity. Then the asymptotic form of the second pair of wavenumbers also takes the form $k_{11,12} \to \mp i\, l$. This corresponds to the Rayleigh varicose mode, with the solution localized at the outer edge of the flow ($x = 1$) and exhibiting exponential decay on both sides of the localization level, both toward the coast and toward the open ocean. In this asymptotic limit, equation (18) can be solved analytically:

$$c_{w1} \to \frac{1 \pm i\sqrt{\tanh l}}{1 + \tanh l}, \quad k_{11,12} \to \mp i\, l, \quad k_{3,2} \to \mp i\, l \tag{19}$$

Equation (19) corresponds to equation (23) from Rayleigh's book (1926, Chapter 21, paragraph 365, equation 23). This asymptotic solution for the upper plus sign is shown in Figure 2a with a dashed line.

2. If $c \to 1$, it may happen that the expression $4(c-1)^2 l^2$ under the square root in formula (8) tends to zero faster than $b^2 \to 0$. Then the asymptotic form of the root is $\left(b - 2(c-1)^2 l^2 / b\right)$. As a result, we obtain the following asymptotics for the wavenumbers:

$$c_{w2} \to 1, \quad k_{11} \to -\frac{b}{(c_{w2}-1)}, \quad k_{12} \to -\frac{(c_{w2}-1)l^2}{b}, \quad k_{3,2} \to \mp i\, l. \tag{20}$$

Using Table 1, it is easy to verify the correctness of this asymptotic result.

Table 1. Western Boundary Current. Values of meridional phase velocity and zonal wavenumbers k_{11}, k_{12}, k_2, k_3 at $\beta = 0.01$ and meridional wavenumbers $l = 0.04, 0.07, 0.1, 0.5, 1$. The numerical results obtained in (Fantini and Tung, 1987) are indicated by color.

	l	c	k_{12}	k_{11}	k_2	k_3
Fantini and Tung, 1987	0.04	1.030 + 0.005 i	-1.920e-4 - 3.200e-5 i	-8.1079 + 1.3514 i	-0.2359 + 0.0012 i	-0.0068 - 0.0000 i
Our computational results		1.0298 + 0.0060 i	-1.907e-4 - 3.865e-5 i	-8.0585 + 1.6329 i	-0.2360 + 0.0015 i	-0.0068 - 4.210e-5 i
Fantini and Tung, 1987	0.07	1.0843 + 0.1971 i	-0.0028 - 0.0067 i	-0.2591 + 0.6194 **i**	-0.0838 + 0.0486 i	-0.0438 - 0.0254 i
Our computational results		1.0837 + 0.1966 i	-0.0028 - 0.0067 i	-0.2590 + 0.6219 i	-0.0838 + 0.0485 i	-0.0438 - 0.0253 i

Fantini and Tung, 1987	0.1	0.9910 + 0.2760 i	0.0007 - 0.0258 i	0.0111 + 0.3877 i	-0.0536 + 0.1026 i	-0.0400 - 0.0765 i
Our computational results		0.9906 + 0.2763 i	0.0008 - 0.0258 i	0.0115 + 0.3873 i	-0.0537 + 0.1027 i	-0.0400 - 0.0765 i
Our computational results	0.5	0.6907 + 0.4649 i	0.0096 - 0.4852 i	0.0102 + 0.5150 i	-0.0101 + 0.5067 i	-0.0098 - 0.4932 i
Our computational results	1	0.5699 + 0.4954 i	0.0050 - 0.9943 i	0.0050 + 1.0058 i	-0.0050 + 1.0043 i	-0.0050 - 0.9957 i

c. Analytical expression for the zonal displacement and velocity field

To construct the plots, we explicitly write out the formulas for the zonal displacement:

$$\begin{aligned}
\eta_1 &= \exp\left(ik_2\left(x-1\right)\right)\left[\exp\left(i\,k_{12}\right)-\exp\left(i\,k_{11}\right)\right]\exp\left(i\,l\,y\right), \quad x \geq 1, \\
\eta_2 &= \left[\exp\left(i\,k_{12}x\right)-\exp\left(i\,k_{11}x\right)\right]\exp\left(i\,l\,y\right), \quad 0 \leq x \leq 1.
\end{aligned} \quad (21)$$

Formulas for the zonal velocity $\left(u=-\Phi_{,y}\right)$:

$$u_1 = -i\,l\,c_w\left\{\exp\left[i\,k_2\left(x-1\right)\right]\right\}\left[\exp\left(i\,k_{12}\right)-\exp\left(i\,k_{11}\right)\right]\exp\left(i\,l\,y\right), \quad x \geq 1. \quad (22)$$

Formulas for the meridional velocity in the outer region $\left(v=\Phi_{,x}\right)$:

$$v_1 = i\,k_2\,c_w\left\{\exp\left[i\,k_2\left(x-1\right)\right]\right\}\left[\exp\left(i\,k_{12}\right)-\exp\left(i\,k_{11}\right)\right]\exp\left(i\,l\,y\right), \quad x \geq 1. \quad (23)$$

The overall time factor $\exp\left(-i\,\omega\,t\right)$ is omitted in all three formulas.

5. Eastern Meridional Boundary Current

Now, conversely, we discard the right half of the jet solution (7), and instead of the right boundary condition at $x=1$, we place a rigid wall at the center $\left(\Phi_2 = 0, \quad x=0\right)$, from which we again find $B=-A$. The solution takes the form

$$\begin{aligned}
\Phi_2 &= \left(c_e-1\right)\left[\exp\left(ik_{12}x\right)-\exp\left(ik_{11}x\right)\right], \quad -1 \leq x \leq 0, \\
\Phi_3 &= c_e\left\{\exp\left[ik_3\left(x+1\right)\right]\right\}\left[\exp\left(-ik_{12}\right)-\exp\left(-ik_{11}\right)\right], \quad x \leq -1, \quad \text{Im}\left(k_3\right) \leq 0..
\end{aligned} \quad (24)$$

The dispersion relation takes the form

$$\left[\left(c_e-1\right)^2 k_{12} - c_e^2\,k_3 - b\right]\exp\left(-i\,k_{12}\right) = \left[\left(c_e-1\right)^2 k_{11} - c_e^2 k_3 - b\right]\exp\left(-i\,k_{11}\right). \quad (25)$$

For the eastern boundary layer, the asymptotic form of the dispersion relation (25) at $\left(\beta \to 0, \quad l > 0\right)$ also takes the form

$$c_e \to \frac{1 \pm i\sqrt{\tanh l}}{1 + \tanh l} \qquad (26)$$

The formulas for the zonal displacement take the form

$$\eta_2 = \left[\exp\left(i\,k_{12}x\right) - \exp\left(i\,k_{11}x\right)\right]\exp\left(i\,l\,y\right), \quad -1 \le x \le 0,$$

$$\eta_3 = \exp\left(ik_3\left(x+1\right)\right)\left[\exp\left(-i\,k_{12}\right) - \exp\left(-i\,k_{11}\right)\right]\exp\left(i\,l\,y\right), \quad x \le -1. \qquad (27)$$

Formulas for the zonal velocity $\left(u = -\Phi_y\right)$:

$$u_3 = -i\,l\,c_e\left\{\exp\left[i\,k_3\left(x+1\right)\right]\right\}\left[\exp\left(-i\,k_{12}\right) - \exp\left(-i\,k_{11}\right)\right]\exp\left(i\,l\,y\right), \quad x \le -1. \qquad (28)$$

Formulas for the meridional velocity in the outer region $\left(v = \Phi_x\right)$:

$$v_3 = i\,k_3\,c_e\left\{\exp\left[i\,k_3\left(x+1\right)\right]\right\}\left[\exp\left(-i\,k_{12}\right) - \exp\left(-i\,k_{11}\right)\right]\exp\left(i\,l\,y\right), \quad x \le -1. \qquad (29)$$

The overall time factor $\exp\left(-i\,\omega\,t\right)$ is omitted in all three formulas.

6. Numerical Solutions

The results of the numerical solutions are presented in Figs. 1–8, as well as in the Supplementary Figures S1–S7. The linear model equations were solved using a direct numerical integration method based on the precise calculation of their values in the complex plane. These calculations were performed using the MATLAB environment. Specifically, the dispersion relations, which are transcendental equations in the complex plane, were solved using MATLAB's built-in optimized functions for finding roots of nonlinear systems. The vpasolve function [https://www.mathworks.com/help/symbolic/sym.vpasolve.html] was adapted for working with complex variables, which enabled us to achieve the required accuracy in determining eigenvalues. Thus, we did not employ any specialized code developed by third-party authors, but rather applied standard and well-verified MATLAB tools for the direct numerical solution of the posed problem.

The numerical results obtained in the present study show good agreement with data from other authors. For comprehensive verification, we additionally supported our numerical solutions with an analytical investigation of the asymptotic behavior and the construction of two-dimensional flow field plots. In particular, we performed calculations for both the western and eastern boundary currents at $\beta = 0.01$, similarly to Fantini and Tung (1987), (see Fig. 2a,b). The values obtained are presented in Table 1. We confirm the results of Hristova et al. (2008), showing that in the region of small wavenumbers ($l \ll 1$), there are no real or imaginary roots corresponding to stable modes. As the wavenumber increases to $l = 0.07$, the accuracy improves slightly, reaching approximately 0.1. However, achieving acceptable accuracy requires higher wavenumber values, at which the error in root determination significantly decreases.

Figure 2 shows the results of numerical solutions for the western and eastern boundary currents (see Eqs. (18) and (25)). The dashed lines represent the solution at $\beta = 0$ – the Rayleigh varicose mode (Gnevyshev et al., 2025). It is evident that the influence of β appears in the long-wave part of the spectrum (small longitudinal wavenumbers l). A comparison of Fig. 2a and Fig. 2b clearly shows the anisotropic effect of the β parameter on the western and eastern boundary

currents. For the western current (Fig. 2a), the β parameter has a stabilizing effect (the imaginary part of the phase speed decreases, the red curve in Fig. 2a lies below the dashed red curve, and the waves become almost neutral) on the Rayleigh varicose mode. In contrast, for the eastern current (Fig. 2b), the β parameter destabilizes the solution in the long-wave range almost explosively (the red curve in Fig. 2b lies above the dashed red curve at the beginning of the coordinates). Considering that the real ocean has some finite viscosity (Fantini and Tung, 1987), the manifestation of long Rossby waves in the western boundary current becomes unlikely. Conversely, for the eastern boundary current, the influence of the β parameter produces a local maximum for the growth increments in the long-wave part of the spectrum (see Figs. S3, S4, S5), making the detection of Rossby waves in the eastern boundary current quite realistic. The spectral curve values at key points of the two-dimensional plots are presented in Tables 1 and 2. The eigenvalues at reference points show good agreement of our calculations with the data of Fantini & Tung (1987) and Hristova et al. (2008) (see Supplementary Figs. S1, S2, S3, S4). However, the principal advantage of our numerical solutions is that we construct two-dimensional sections of the real part of the eigenfunction, rather than one-dimensional cross-sections perpendicular to the flow, as was done in Fantini and Tung (1987) and Hristova et al. (2008). We also pay attention to the wavenumbers within the flow itself (see Supplementary Figs. S2, S5), which are an important aspect for understanding radiation into the open ocean.

Table 2. Eastern Boundary Current. Values of meridional phase velocity and zonal wavenumbers k_{11}, k_{12}, k_2, k_3 at β = 0.01 and meridional wavenumbers l = 0.01; 0.04; 0.07; 0.1; 0.5; 1.

l	c	k_{11}	k_{12}	k_2	k_3
0.01	0.2858 + 0.4489 i	1.0037 + 0.6309 i	7.1415e-5 - 4.4891e-5 i	-1.0094 + 1.5851 i	-2.8583e-5 - 4.4885e-5 i
0.04	0.6477 + 0.2911 i	0.4194 + 0.3503 i	0.0022 - 0.0019 i	-0.3169 + 0.1463 i	-0.0042 - 0.0019 i
0.07	0.7577 + 0.2385 i	0.2914 + 0.3031 i	0.0081 - 0.0084 i	-0.1435 + 0.0671 i	-0.0280 - 0.0131 i
0.1	0.8261 + 0.2766 i	0.1487 + 0.2866 i	0.0143 - 0.0275 i	-0.0659 + 0.1048 i	-0.0423 - 0.0684 i
0.5	0.6771 + 0.4649 i	0.0104 + 0.5146 i	0.0098 - 0.4856 i	-0.0102 + 0.5068 i	-0.0099 - 0.4931 i
1	0.5655 + 0.4954 i	0.0050 + 1.0057 i	0.0050 - 0.9943 i	-0.0050 + 1.0044 i	-0.0050 - 0.9956 i

A crucial point we focus on is that the wavenumbers within the jet are never truly complex-conjugate. Without these calculations, one could only establish that the imaginary parts of these wavenumbers form pairs with opposite signs. However, our numerical analysis shows that the wavenumbers $k_{1,1}$, $k_{1,2}$ and k_2, k_3 do indeed have imaginary parts of opposite sign, but at small wavenumbers they are not complex-conjugate, and in the long-wave range they are significantly separated in magnitude. They approach the complex-conjugate regime for meridional wavenumbers only when $l > 0.5$, at which point the β-effect becomes negligible, and the solution takes the form of the Rayleigh varicose mode (Gnevyshev et al., 2025). Qualitatively, this behavior is characteristic of nearly all cases considered in this paper. This can also be seen in Tables 1–2 and in the graphs of Supplementary Figs. S2, S5.

The plot of zonal displacement at β = 0.01, l = 0.05 exhibits a quasi-one-dimensional structure characteristic of a quasi-neutral Rossby wave (Supplementary Fig. S6). In the quasi-geostrophic approximation, the velocity field shows alternating bands of flow oriented nearly

meridionally. As the wavenumber increases, the imaginary part of the phase speed c also increases (see Supplementary Fig. S7), along with the imaginary part of the wavenumber k, perpendicular to the flow (i.e., the imaginary part of the zonal wavenumber). Consequently, instead of quasi-neutral Rossby waves — i.e., shear flows propagating infinitely far from the flow boundary—unstable Rossby waves (vortices) emerge, becoming increasingly localized at the outer edge of the flow, i.e., in the vorticity layer, and eventually transition into the Rayleigh vortex mode.

Figures 3 and 4 show the spatial structure of the velocity field of perturbations in the western boundary current for $\beta = 0$ and $\beta = 0.01$ at three values of the longitudinal wavenumber l = 0.04; $l = 0.07$, and $l = 0.1$. The axes display normalized spatial coordinates x and y. Arrows represent the velocity vector field in the x–y plane, while the background color indicates the sign of vorticity: red for cyclonic (region L) and blue for anticyclonic (region H). The disturbances exhibit a fairly large-scale structure with clearly defined alternating cyclonic and anticyclonic regions of vorticity aligned along the boundary. For $l = 0.04$, the perturbations are localized in a wide coastal band, corresponding to a slowly decaying mode. As l increases, the vortex size decreases, and the structure becomes more compressed toward the boundary. There is a tendency to form more distinct vortex cells. Spatial localization intensifies: perturbations are concentrated closer to the boundary. With increasing longitudinal wavenumber, coastal localization is further enhanced, and the scale of the vortices diminishes. These features indicate a suppression of effective Rossby wave radiation on the western side.

For $\beta = 0.01$, the velocity distribution at $l = 0.04$ (Fig. 4a) significantly differs from that at zero β (compare Figures 3a and 4a): the perturbations appear as nearly sinusoidal waves across the width, with a uniform alternation of directions and without pronounced vorticity; the solution retains a quasi-harmonic character, and the structure resembles a Rossby wave with minimal dispersion. However, at $l = 0.07$ (compare Figures 3b and 4b, which show little difference), the influence of the beta parameter is already negligibly small, and a distinct vortex structure emerges, with alternating H and L regions aligned along the boundary. The vortices are localized closer to the coast, but they are less concentrated compared to the previous case (see Fig. 3). At $l = 0.1$ (Fig. 4c), vortex localization becomes more pronounced, yet the vorticity zones remain elongated along the x-axis, indicating continued propagation; the structure increasingly resembles classical barotropic modes of the boundary layer with characteristic phase variations in latitude. Thus, the β parameter promotes more effective propagation of perturbations from the coastal zone into the open ocean only in the longwave range.

The eigenvalues for the first and second modes of the eastern meridional boundary current were computed for $\beta = 0.5$ (see Supplementary Figs. S3 and S4). Panels (a) show the real (RE) and imaginary (IM) parts of the phase speed c, while panels (b) display the absolute values of the imaginary part ($c_i\, l$), characterizing the growth (or decay) amplitude of the modes, as a function of the dimensionless longitudinal wavenumber l.

In the plot for the first mode, the real part Re increases monotonically with l, starting from negative values and reaching positive values for $l > 0.1$ (Fig. S3a). This indicates a transition of the wave from propagating in one direction to the opposite as the longitudinal inhomogeneity increases. The imaginary part is positive at small l, reaching a maximum around $l \approx 0.05$, and then decreases toward zero, indicating the presence of instability at low wavenumbers. In the plot for the first mode (Fig. S3b), ($c_i\, l$) decreases and becomes nearly zero for $l > 0.2$, meaning the first mode is unstable only within a limited wavelength range. The real part of the second mode (Fig. S4a) also increases with l, but the curve shape differs significantly from that of the first mode:

14

there is an initial plateau followed by growth. The imaginary part is much smaller at low l but shows a steady increase with increasing wavenumber, as clearly seen in panel Fig. S4b. This indicates that the second wave becomes unstable at higher l, unlike the first mode, whose instability is confined to small l.

A comparison of the plots for the two waves shows that the mechanisms of their instability are fundamentally different: the first mode exhibits instability in the long-wave range, whereas the second wave is unstable in the short-wave range. This indicates the presence of a spectrum of instabilities of different nature, associated both with large-scale and small-scale dynamics. Such behavior is characteristic of the eastern meridional current with a negative planetary vorticity gradient and underscores the importance of modal analysis when studying radiating instabilities.

Figure 5 shows the spatial structures of the velocity vector field for the eastern boundary current at a fixed parameter value of $\beta = 0.01$ and for various values of the wavenumber l. Black arrows indicate the direction and relative magnitude of the velocity, while the colored regions correspond to vorticity zones: red (labeled "H") – anticyclonic, blue (labeled "L") – cyclonic. In the long-wave regime ($l = 0.04$, Fig. 5a), the velocity field exhibits an almost laminar character with pronounced meridional variability, where velocities reverse direction. Velocities are predominantly aligned along the x-axis, symmetrically with respect to $y = 0$. Vorticity is practically absent, indicating a stable and weakly perturbed flow. As the wavenumber increases to $l = 0.07$ (Fig. 5b), a periodic structure emerges with alternating zones of cyclonic and anticyclonic vorticity. Vortical formations become clearly pronounced, their scale corresponding to the spatial scale of the perturbations. The velocity field deviates from linearity, reflecting rotational motion and indicating the development of instability and the appearance of wave perturbations localized near the boundary of the current. For the high-frequency regime ($l = 0.5$, Fig. 5c), there is even stronger localization of the vortical structures. The alternating H and L regions become compact, with well-defined boundaries and high vorticity intensity. The vector field shows a significant deviation from linearity, pointing to enhanced wave processes, especially in the coastal zone. Thus, with increasing wavenumber, there is a transition from a stable laminar flow to a state with pronounced vortical activity and structural heterogeneity.

Figure 6 shows the distributions of zonal displacement for the eastern boundary current at $\beta = 0.01$, $l = 0.07$. It is evident that the zonal displacements strongly depend on the wavenumber l. As the wavenumber increases, the perturbations become localized near the coastal boundary and are practically absent in the central part of the considered region.

Figure 6 shows the distributions of zonal displacement for the eastern boundary current at $\beta = 0.01$, $l = 0.07$. Figure 6 illustrates the spatial structure of the zonal displacement at different display scales along the x-axis. At a broad scale (Fig. 6a), the wave-like structure of the zonal displacement is clearly visible, manifesting as alternating elongated zones of positive and negative values. This indicates the presence of quasi-periodic fluctuations along the current, likely associated with the wave nature of the instabilities. At a medium scale (Fig. 6b), the displacement distribution within the inner part of the current can be examined in greater detail. Here, asymmetry along the meridional coordinate is particularly noticeable: the amplitude of oscillations increases toward the central part of the flow. This may be related to the enhanced influence of boundary effects and dynamics deviating from strict zonality. At the local scale (Fig. 6c), it can be seen that even near the current boundary, significant displacement persists, and it is asymmetric with respect to the jet axis. The presence of such local fluctuations may be linked to the generation of small-scale vortices or internal modes modulating the main flow. The pronounced zonal structure at all

three scales, especially in panel (a), confirms the existence of radiating modes capable of transporting energy over long distances.

Calculations of the zonal displacement for both the eastern and western boundary currents at a significantly larger wavenumber, $l = 0.5$ (instead of $l = 0.07$; with the parameter β unchanged: $\beta = 0.01$), show a pronounced flattening of the distribution along the x-axis: the zonal displacement is concentrated near the very edge of the current (not shown). This indicates that at larger l the perturbation energy is less effectively radiated outward and remains localized near the main jet. The zonal displacements exhibit a clear harmonic (wave-like) structure, almost perfectly symmetric with respect to the axis $y = 0$. This suggests that at large l, perturbations do not develop as "radiating modes" but rather take the form of stationary, confined structures (vortices). Strong attenuation along the x-axis is observed. This means that at higher l the radiation mechanism is practically suppressed, and the energy remains confined within the main circulation zone.

The visualizations of zonal displacement confirm a key theoretical hypothesis: the meridional tilt of the jet plays a decisive role in the formation and nature of instabilities. At small values of l, the flow allows the development of radiating modes capable of transferring energy over long distances and forming autonomous mesoscale structures (vortices). At large values of l, perturbations remain localized, circulation is confined, and the energy "radiation" effect is absent. This underscores the importance of accounting for the jet geometry (particularly its tilt) when modeling and interpreting oceanic boundary currents. The additional branches of the spectral problem obtained by Hristova et al. (2008) do not qualitatively yield any novel insights. We have constructed velocity fields for characteristic values corresponding to their findings presented in Figures 7 and 8.

Figure 7 shows the velocity fields for the first mode of the eastern boundary current at $\beta = 0.5$ for different values of the wavenumber l. For $l = 0.348$, the velocity field is characterized by alternating bands of flow predominantly oriented in the meridional direction. Zones with varying velocity vector directions are observed, but their spatial structure retains the order typical of linear modes. As the wavenumber increases to $l = 0.5$, the velocity vectors tilt more noticeably, indicating stronger rotational components in the flow. The flow structure acquires a diagonal orientation, reflecting a transition from a primarily zonal flow to a regime with a pronounced meridional component. The most significant changes occur at $l = 1$, where stable vortical structures form, clearly marked by regions of anticyclonic (B) and cyclonic (H) vorticity. The flow pattern takes on a quasi-closed form typical of vortex cells. The emergence of such structures indicates enhanced instabilities in the boundary layer and a potential transition to more complex nonlinear dynamics.

For the second mode of the eastern boundary current (Fig. 8), the velocity field structure differs significantly from that of the first mode. At a small wavenumber, the flow retains a predominantly zonal character, although a clearer alternation of velocity vector directions is observed in the vertical direction. As the wavenumber increases, well-defined vortical structures emerge, with alternating regions of anticyclonic (B) and cyclonic (H) vorticity. Compared to the first mode, these structures extend further in the longitudinal direction, and the vortex amplitude is higher, indicating a more pronounced instability and greater spatial organization of the second mode. At $l = 1$, the vortex cells become more compact but maintain a regular alternation similar to the first mode. However, the meridional scale of the vortices in the second mode is smaller than in the first, reflecting a more complex modal structure of the flow. Thus, the second mode is characterized by a more intricate meridional structure and a higher degree of vortical organization

compared to the first mode, indicating a higher-frequency nature of the perturbations and their influence on the flow structure.

The zonal distributions for the first mode at β = 0.5 (not shown) confirm that at higher values of the β parameter, the perturbations acquire a pronounced coastal character. Similar patterns are observed for the second wave (not shown). The spatial structure of the zonal displacement demonstrates an increase in oscillation amplitude in the coastal zone, accompanied by a sharper decay of intensity toward the open ocean. This indicates that the effect of planetary vorticity gradients significantly enhances the coastal localization of modal structures. Additionally, a shift of the displacement maxima closer to the coast is observed with increasing β and l, pointing to a growing contribution of local dynamic mechanisms, such as the β-plane effect and the influence of boundary conditions. Taken together with the previous figures, these results suggest a high sensitivity of the eastern boundary current structure to dispersion parameters and latitude-dependent rotational components.

7. Interpretation of the theoretical model for the Lofoten Basin

For the interpretation of the theoretical model, we considered a topographically isolated feature – the Lofoten Basin of the Norwegian Sea, which is bounded to the northwest by the Mohn Ridge, to the southwest by the Helgeland Ridge, to the south by the Vøring Plateau, and to the east by the continental slope of the Scandinavian Peninsula. Its waters cover the area between 2° W and 10° E, 68° and 72° N. To the west of the Mohn Ridge lies the Greenland Basin, and to the west of the Helgeland Ridge is the Norwegian Basin (Fig. 9).

Our choice of the Lofoten Basin for this study is dictated by its unique hydrodynamic structure. Despite its regional character, it represents an ideal testbed for interpreting our theoretical model. By "interpreting" the analytical model, we aim to assess its ability to qualitatively and, where possible, quantitatively reproduce observed dynamic features in a relevant natural system. The Lofoten Basin effectively mimics a system of western and eastern boundary currents, thereby allowing us to investigate asymmetries in radiating modes. Success would be indicated by the model's capacity to predict the distinct characteristics and behaviors of these "analogue" boundary currents and their associated wave radiation patterns, such as their spatial structure, amplitude distribution, and the mechanisms of energy transfer, in a manner consistent with observations from the Lofoten Basin. Conversely, failure would imply a significant divergence between model predictions and observed dynamics, or an inability to capture the fundamental physical processes at play.

The key elements of this system are the Norwegian Slope Current (NSC) and the Norwegian Atlantic Front Current (NAFC), which essentially form the "walls" of the basin.

The NSC, located along the continental slope/Norwegian shelf, constitutes the eastern boundary of the basin. This is a relatively swift jet, topographically "trapped" to the slope, exhibiting strong topographic control and pronounced meridional transport of Atlantic Water. On a local scale, the NSC functions as a dynamic analogue of an eastern boundary current.

Conversely, the NAFC is situated in the open part of the basin, forming its western boundary, opposite the shelf. It represents a band with a strong frontal (gradient) structure of density and velocities, less rigidly coupled to the bottom topography compared to the NSC. The NAFC thus serves as a dynamic analogue of a western meridional branch.

It is crucial to emphasize that our usage of the terms "western" and "eastern" boundary currents in the context of the Lofoten Basin constitutes a dynamic analogy, rather than being part of a global classification of subtropical gyres. This local dynamic analogy, where the NSC acts as an analogue for an eastern boundary current on the "eastern wall" and the NAFC as an analogue for a western boundary current on the "western wall," makes the Lofoten Basin an exceptionally valuable object for studying regional manifestations of the principles described by our model for global systems. Therefore, this is not an official classification, but rather a deliberate selection of a region possessing the necessary dynamic characteristics to test our hypothesis regarding the asymmetry between western and eastern boundary currents.

As shown by Fantini and Tung (1987) and Hristova et al. (2008), the presence of a meridional tilt in the jets plays a decisive role in shaping the spectrum of possible perturbations and their ability to propagate over long distances. One of the most important characteristics of such currents is the emergence of so-called *radiating instabilities* of the modes, whose energy does not remain confined within the generation region but can propagate beyond it, affecting distant parts of the ocean. In the case of strictly zonal currents, such modes are impossible: even if instability develops, the resulting perturbations remain localized, and their energy does not extend beyond the main jet. In contrast, in currents with a deviation from zonality, the presence of a meridional component creates conditions for the formation of wave solutions that can efficiently radiate from the main circulation region, carrying energy over significant distances.

We used the high-resolution GLORYS12V1 global ocean reanalysis to validate our theoretical model. The GLORYS12V1 product is a data-assimilated eddy-resolving global reanalysis (1/12° horizontal resolution and 50 vertical levels), publicly available from the Copernicus Marine Environment Monitoring Service at http://marine.copernicus.eu. Observations, such as in situ temperature and salinity profiles, satellite sea surface temperature, and along-track sea level anomalies from satellite altimetry, are assimilated to simulate the evolution of the physical ocean properties. The data assimilation method used is a reduced-order Kalman filter. The numerical model used is the Nucleus for European Modeling of the Ocean (NEMO) general circulation model with model surface boundary conditions derived from the European Center for Medium-Range Weather Forecasts (ECMWF) atmospheric reanalysis and forecasts.

We used the "Mesoscale Eddy Trajectory Atlas 3.2 Delayed Time all-satellites" (META3.2 DT allsat) product, available at https://www.aviso.altimetry.fr/, is used. This product is based on the use of altimetric information (sea surface height) for identifying and tracking the trajectories of cyclones and anticyclones in the World Ocean (Pegliasco et al., 2022). The algorithm identifies and tracks isolated eddies on daily maps, recording their evolution over time. The atlas assigns each eddy a unique identification number and its trajectory coordinates. The META3.2 product contains information about eddy type, radius, amplitude, orbital velocity, and lifespan.

For describing the bottom relief, the global digital elevation model ETOPO1 (Earth Topography and Bathymetry) is used, which integrates information on topography, bathymetry, and coastline from high-resolution regional and global datasets.

This radiation mechanism, linked to the geometry of the jet, has important implications for the formation of mesoscale eddies. Waves leaving the boundaries of the main jet can transform into localized quasi-geostrophic structures – eddies – which then continue to exist autonomously.

Figure 10 illustrates the spatial distribution of velocities and directions of surface currents within the Lofoten Basin. Arrows indicate velocity vectors, while the numbers show the jet width in kilometers (between the ticks), allowing an assessment of the variability of the circulation

structure in this area. Analysis of Figure 10 shows that the main current follows the eastern periphery of the basin, tracing the outline of the continental slope of the Scandinavian Peninsula. It is characterized by significant velocities and a relatively narrow jet width (70–90 km), corresponding to the Norwegian Slope Current. In the western part of the basin, the current bends around the Mohn Ridge. Here the jet is wider (over 200 km) and has less pronounced velocity maxima, consistent with the characteristics of the Norwegian Front Current. Within the Lofoten Basin, there is a region of reduced velocity (with a width of about 205 km), where the flow is weaker and less organized. This aligns with the fact that the central part of the basin is a zone of interaction and redistribution of flows. Jet widths range from ~70 km (in the east) to over 200 km (in the central and western parts), indicating the strong influence of topography on the formation of circulation structures. The overall direction of water movement corresponds to the advection of Atlantic waters toward the northeast, heading toward the Arctic, in agreement with the large-scale pattern of the Norwegian Atlantic Current.

Figure 11 shows the trajectories of mesoscale eddies formed along the western (left panels) and eastern (right panels) boundary currents in the Lofoten Basin area. The color scale indicates the direction of eddy movement, while the isobaths (at 1000 m intervals) allow assessment of the influence of bottom topography on the displacement of these structures. Analysis of the figure reveals that the anticyclonic eddies generated in the eastern (slope) boundary current exhibit predominantly northwestward and westward advection (zonal displacement), with extended trajectories often crossing the central part of the Lofoten Basin. In contrast, eddies formed in the western (front) boundary current display more limited trajectories (zonal displacements). Their propagation suggests a relatively weak capacity to reach the central regions of the basin.

Thus, the presence of a meridional tilt of the jets proves to be a key factor: it determines the spectrum of radiating instabilities capable of remotely transporting energy from the main circulation flow and transforming into mesoscale eddies. To demonstrate the applicability and validity of our theoretical model, and for comparison with theoretical estimates of the meridional boundary currents (BC) in the Lofoten Basin – the Western BC (NAFC) and Eastern BC (NSC) – Tables 3 and 4 were compiled. Table 3 demonstrates that the estimated $\beta^* = 0.01$ (Fantini and Tung, 1987) exhibited better agreement with observed reality compared to the estimate of $\beta^* = 0.5$ (Hristova et al., 2008).

Table 3. Values of β and β^*, widths (km), and current velocities (cm/s) for the Western Boundary Current (WBC) and Eastern Boundary Currents (EBC) in the Lofoten Basin as a function of latitude.

Latitude (°N)	$\beta \times 10^{11}$	Current width (km)		Current velocity (in the core) (cm/s)		β^*	
		WBC	EBC	WBC	EBC	WBC	EBC
72	0.7057	240	72	13	18	0,0313	0,0020
71.75	0.7151	191	69	8	18	0,0326	0,0019
71.5	0.7246	140	81	13	18	0,0109	0,0026
71.25	0.7341	214	85	16	18	0,0210	0,0029
71	0.7435	173	79	14	22	0,0159	0,0021
70.75	0.7529	102	73	13	24	0,0060	0,0017
70.5	0.7623	103	85	13	27	0,0062	0,0020
70	0.7811	106	83	8	42	0,0110	0,0013
69.75	0.7904	96	76	11	50	0,0066	0,0009
69.5	0.7998	77	91	11	33	0,0043	0,0020
69.25	0.8091	117	98	13	50	0,0085	0,0016

69	0.8184	115	75	8	44	0,0135	0,0010
The average value for 69°-72°N	0.7614	140	81	12	30	0,0140	0,0018

Table 4 presents the mean number of eddies and their characteristic sizes for WBC and EBC, calculated using META3.2 data. A good agreement with theoretical predictions is observed. Specifically, the number of eddies in the eastern region is approximately double that in the western region. Furthermore, the eddy sizes are consistent with the short-wave regime wave numbers predicted by the analytical model. Notably, eastern eddies are marginally larger than their western counterparts, which also aligns with the results of the analytical model.

Table 4. Parameters of long-lived (> 10 days) cyclones (CEs) and anticyclones (AEs) according to META 3.2DT data for 1993-2021 in the Lofoten Basin.

Boundary Current	WBC (NAFC)		EBC (NSC)	
The polarity of eddies	AEs	CEs	AEs	CEs
Number of eddies	1630	1472	2251	2536
Duration of life (days)	29.58±25.01	29.18±24.31	28.45±25.82	27.77±21.97
Displacement (km)	50.06±42.25	51.15±41.33	63.19±54.28	58.58±47.12
Path (km)	145.35±127.83	144.22±127.18	165.08±150.89	166.37±138.69
Displacement speed (cm/s)	2.30±1.55	2.42±1.59	3.06±2.07	2.90±1.98
Path speed (cm/s)	5.69±1.97	5.69±1.91	6.79±2.39	6.93±2.31
Radius (km)	32.51±6.31	31.70±6.55	35.49±7.26	34.79±6.75
Amplitude (cm)	2.48±1.06	2.43±1.27	3.19±1.81	3.00±1.47

8. Conclusions and Discussion

1.   The spectral problem can be conventionally divided into two regions: the long-wave region ($l < 0.5$) and the short-wave region ($l > 0.5$), where l is the meridional wavenumber normalized by the jet width. In the long-wave part of the spectrum ($l < 0.5$), quasi-monochromatic Rossby waves are radiated into the open ocean, and there is a clear asymmetry between the western and eastern boundary currents. The western boundary current emits Rossby waves with small growth rates. The wavenumber and group velocity of the Rossby waves radiated into the open ocean are almost zonal and oppositely directed (the phase propagates westward while the group velocity is directed eastward). In contrast, the eastern current emits Rossby waves with larger growth rates. The wavenumber is oriented almost meridionally, and the group velocity is directed nearly westward. The Rossby waves radiated by the eastern current are approximately twice as long as those emitted by the western current.

2.   A subtler aspect, which has largely eluded all previous authors, is the structure of the solution within the jet itself. Numerical calculations revealed the following picture. In the long-wave part of the spectrum ($l < 0.5$), the wavenumbers $k_{1,1}$ and $k_{1,2}$ inside the jet are widely separated in both their real and imaginary parts (although their product always equals the square of the meridional wavenumber and is positive) (see Tables 1 and 2, as well as Supplementary Figs. S2 and S5). This results in wave vectors inside the jet failing to form a pure classical mode within the flow. Instead, an unbalanced flux arises, propagating from the coast toward the open ocean. This unbalanced wave, moving toward the open ocean, undergoes refraction at the jet's outer boundary

(the boundary behaves like an interface between media with different refractive indices) and is radiated into the open ocean as a quasi-monochromatic Rossby wave.

In the short-wave region ($l > 0.5$), the wave vectors within the jet gradually converge to purely imaginary, self-conjugate values. The phase propagating across the jet disappears, meaning that nothing is radiated into the open ocean, and only the balanced classical mode remains within the flow. This solution is commonly referred to as the Rayleigh "varicose mode" (half-mode).

Consequently, the radiation of Rossby waves in the long-wave range of non-zonal currents originates primarily from the coast rather than being emitted by the jet itself. At the outer boundary, the wave coming from the coast undergoes refraction. In the short-wave range, the vortices appearing at the outer boundary of the jet are a consequence of the barotropic instability of the jet itself.

3. Our numerical results corroborate the findings of other authors (in particular, Fantini & Tung, 1987; Hristova et al., 2008). We verified and identified additional modes (see Supplementary Figs. S1, S3, S4), which were observed at $\beta = 0.5$ in Hristova et al. (2008). A possible reason for the appearance of these additional branches in the dispersion relation, we believe, may be an improper formulation of the problem. The fact is that for Rossby waves in the meridional (non-zonal) jet, there is not a single pair but two pairs of waves propagating in opposite directions—two classical waves and two waves with negative energy (for which the phase propagates eastward rather than westward) (Gnevyshev et al., (2020). Between these pairs of waves lies a critical layer. Consequently, during the numerical calculation of wavenumbers, the computational algorithm cannot determine which specific waves to select within the jet. As a result, we observe the emergence of up to four branches in the dispersion relation.

4. The parameters used in the numerical solutions (in particular, the value $\beta = 0.01$) are realistic and adequately reflect the physical scales of the Lofoten Basin in the Norwegian Sea. The Mohn and Helgeland ridges, as well as the continental slope, form natural boundaries and guides for circulation, determining the pathways of the boundary currents and creating conditions for the localization of instabilities.

5. The eastern and western boundary currents in the Lofoten Basin differ in their dynamics and mechanisms of eddy generation. The eastern (slope) current, flowing along the continental slope, demonstrates the ability to generate radiating modes accompanied by the formation of anticyclonic eddies capable of propagating over considerable distances. The western (frontal) current, following the submarine ridges, produces eddies with limited trajectory extent, indicating the localized nature of the perturbations.

ACKNOWLEDGMENTS

AUTHOR DECLARATIONS

Conflict of Interest

The authors have no conflicts to disclose.

REFERENCES

Afanasyev, Y. D., O'leary, S., Rhines, P. B., & Lindahl, E. (2012). On the origin of jets in the ocean. *Geophysical & Astrophysical Fluid Dynamics, 106*(2), 113–137. https://doi.org/10.1080/03091929.2011.562896

Arbic, B. K., Scott, R. B., Flierl, G. R., et al. (2012). Nonlinear Cascades of Surface Oceanic Geostrophic Kinetic Energy in the Frequency Domain. *Journal of Physical Oceanography, 42*(9), 1577–1600. https://doi.org/10.1175/JPO-D-11-0151.1

Belonenko, T. V., Bashmachnikov, I. L., & Kubryakov, A. A. (2018). Horizontal advection of temperature and salinity by Rossby waves in the North Pacific. *International Journal of Remote Sensing, 39*(8), 2177–2188. https://doi.org/10.1080/01431161.2017.1420932

Belonenko, T. V., Kubryakov, A. A., & Stanichny, S. V. (2016). Spectral Characteristics of Rossby Waves in the Northwestern Pacific based on Satellite Altimetry. *Izvestiya, Atmospheric and Oceanic Physics, 52*(9), 920–928. https://doi.org/10.1134/S0001433816090073

Belonenko, T. V., Kubryakov, A. A. (2014). Temporal variability of the phase velocity of Rossby waves in the North Pacific. *Sovremennye Problemy Distantsionnogo Zondirovaniya Zemli iz Kosmosa [Modern Problems of Remote Sensing of the Earth from Space], 11*(3), 9–18.

Belonenko, T. V., Sandalyuk, N. V., & Gnevyshev, V. G. (2023). Interaction of Rossby waves with the Gulf Stream and Kuroshio using altimetry in a framework of a vortex layer model. *Advances in Space Research, 71*(5), 2384–2393. https://doi.org/10.1016/j.asr.2022.10.042

Belonenko, T. V., Travkin, V. S., Gnevyshev, V. G., & Kochnev, A. V. (2024). Influence of topography on the movement of mesoscale eddies along the continental slope of the New Zealand Plateau. *Sovremennye Problemy Distantsionnogo Zondirovaniya Zemli iz Kosmosa [Modern Problems of Remote Sensing of the Earth from Space], 21*(6), 253–266. https://doi.org/10.21046/2070-7401-2024-21-6-253-266

Belonenko, T. V., Travkin, V. S., Koldunov, A. V., & Volkov, D. L. (2021). Topographic experiments over dynamical processes in the Norwegian Sea. *Russian Journal of Earth Sciences, 21*, ES1006. https://doi.org/10.2205/2020ES000747

Belonenko, T. V., Volkov, D. L., & Koldunov, A. V. (2018). Shelf waves in the Beaufort Sea in a high-resolution ocean model. *Oceanology, 58*(6), 778–785. https://doi.org/10.1134/S0001437018060024

Berloff, P., & Kamenkovich, I. (2013a). On Spectral Analysis of Mesoscale Eddies. Part I: Linear Analysis. *Journal of Physical Oceanography, 43*(12), 2505–2527. https://doi.org/10.1175/JPO-D-12-0232.1

Berloff, P., & Kamenkovich, I. (2013b). On Spectral Analysis of Mesoscale Eddies. Part II: Nonlinear Analysis. *Journal of Physical Oceanography, 43*(12), 2528–2544. https://doi.org/10.1175/JPO-D-12-0233.1

Bower, A. S., Le Cann, B., Rossby, T., et al. (2002). Directly measured mid-depth circulation in the northeastern North Atlantic Ocean. *Nature, 419*(6907), 603–607. https://doi.org/10.1038/nature01078

Bower, A. S., Lozier, M. S., Gary, S. F., et al. (2009). Interior pathways of the North Atlantic meridional overturning circulation. *Nature, 459*(7244), 243–247. https://doi.org/10.1038/nature07979

Bühler, O. (2009). *Waves and Mean Flows*. Cambridge University Press.

Capet, X., McWilliams, J. C., Molemaker, M. J., and Shchepetkin, A. F. (2008). Mesoscale to submesoscale transition in the California Current System, Part I: Flow structure, eddy flux, and observational tests. *J. Phys. Oceanogr.*, 38, 29–43. DOI: 10.1175/2007JPO3671.1

Charney, J. G. (1990). The dynamics of long waves in a baroclinic westerly current. In *The Atmosphere–A Challenge* (pp. 223–250). Springer.

Chelton, D. B., Schlax, M. G., & Samelson, R. M. (2011). Global observations of nonlinear mesoscale eddies. *Progress in Oceanography, 91*(2), 167–216. https://doi.org/10.1016/j.pocean.2011.01.002

Davey, M. K., & Killworth, P. D. (1989). Flows Produced by Discrete Sources of Buoyancy. *Journal of Physical Oceanography, 19*(9), 1279–1290. https://doi.org/10.1175/1520-0485(1989)019<1279:FPBDSO>2.0.CO;2

Eady, E. T. (1949). Long waves and cyclone waves. *Tellus, 1*(3), 33–52. https://doi.org/10.1111/j.2153-3490.1949.tb01265.x

Fantini, M., & Tung, K.-K. (1987). On Radiating Waves Generated from Barotropic Shear Instability of a Western Boundary Current. *Journal of Physical Oceanography, 17*(8), 1304–1308. https://doi.org/10.1175/1520-0485(1987)017<1304:ORWGFB>2.0.CO;2

Ferrari, R., & Wunsch, C. (2009). Ocean Circulation Kinetic Energy: Reservoirs, Sources, and Sinks. *Annual Review of Fluid Mechanics, 41*, 253–282. https://doi.org/10.1146/annurev.fluid.40.111406.102139

Galperin, B., & Read, P. L. (Eds.). (2019). *Zonal Jets. Phenomenology, Genesis, and Physics*. Cambridge University Press. https://doi.org/10.1017/9781107358225

Gill, A., Green, J., & Simmons, A. (1974). Energy partition in the large-scale ocean circulation and the production of mid-ocean eddies. *Deep Sea Research and Oceanographic Abstracts, 21*, 499–528

Gnevyshev, V. G., & Belonenko, T. V. (2025). Doppler and Non-Doppler Shifts in Dispersion Relations for Rossby Waves and Galilean Invariance. *Russian Journal of Earth Sciences, 25*, ES4006. https://doi.org/10.2205/2025ES001012

Gnevyshev, V. G., Frolova, A. V., & Belonenko, T. V. (2022c). Topographic Effect for Rossby Waves on Non-Zonal Shear Flow. *Water Resources, 49*(2), 240–248. https://doi.org/10.1134/S0097807822020063

Gnevyshev, V. G., Travkin, V. S., & Belonenko, T. V. (2023). Topographic Factor and Limit Transitions in the Equations for Subinertial Waves. *Fundamental and Applied Hydrophysics, 16*(1), 8–23. https://doi.org/10.48612/fpg/92rg-6t7h-m4a2

Gnevyshev, V. G., Travkin, V. S., & Belonenko, T. V. (2025). Instability modes in zonal oceanic currents: β-destabilizing effect and transverse energy radiation. *Physics of Fluids, 37*, 076607. https://doi.org/10.1063/5.0267817

Gnevyshev, V. G., Frolova, A. V., Kubryakov, A. A., Sobko, Yu. V., & Belonenko, T. V. (2019). Interaction between Rossby Waves and a Jet Flow: Basic Equations and Verification for the Antarctic Circumpolar Current. *Izvestiya, Atmospheric and Oceanic Physics, 55*(5), 412–422. https://doi.org/10.1134/S0001433819050074

Gnevyshev, V. G., Badulin, S. I., & Belonenko, T. V. (2020). Rossby waves on non-zonal currents: structural stability of critical layer effects. *Pure and Applied Geophysics, 177*, 5585–5598. https://doi.org/10.1007/s00024-020-02567-0

Gnevyshev, V. G., & Belonenko, T. V. (2022b). Anomalous Behavior of the Vertical Structure Rossby Waves on Non-Zonal Shear Flow in the Vicinity of the Focus. *Physical Oceanography, 29*(6), 567–586. https://doi.org/10.22449/1573-160X-2022-6-567-586

Gnevyshev, V. G., Badulin, S. I., Koldunov, A. V., & Belonenko, T. V. (2021b). Rossby Waves on Non-zonal Flows: Vertical Focusing and Effect of the Current Stratification. *Pure and Applied Geophysics, 178*(8), 3247–3261. https://doi.org/10.1007/s00024-021-02799-8

Gnevyshev, V. G., & Belonenko, T. V. (2022a). Analytical Solution of the Ray Equations of Hamilton for Rossby Waves on Stationary Shear Flows. *Fundamental and Applied Hydrophysics, 15*(2), 8–18. https://doi.org/10.48612/fpg/4eh4-83zr-r1fm

Gnevyshev, V. G., Frolova, A. V., Koldunov, A. V., & Belonenko, T. V. (2021a). Topographic Effect for Rossby Waves on a Zonal Shear Flow. *Fundamentalnaya i Prikladnaya Gidrofizika, 14*(1), 4–14. https://doi.org/10.7868/S2073667321010019

Hogg, N. G., & Johns, W. E. (1995). Western boundary currents. *Reviews of Geophysics, 33*(S2), 1311–1334. https://doi.org/10.1029/95RG00491

Howard, L. N., & Drazin, P. G. (1964). On instability of parallel flow of inviscid fluid in a rotating system with variable coriolis parameter. *Journal of Mathematics and Physics, 43*, 83–99. https://doi.org/10.1002/sapm196443183

Hristova, H. G., Pedlosky, J., & Spall, M. A. (2008). Radiating Instability of a Meridional Boundary Current. *Journal of Physical Oceanography, 38*(10), 2294–2307. https://doi.org/10.1175/2008JPO3853.1

Huang, R. X. (2010). *Ocean Circulation: Wind-Driven and Thermohaline Processes*. Cambridge University Press.

Isachsen, P. E. (2011). Baroclinic instability and eddy tracer transport across sloping bottom topography: How well does a modified Eady model do in primitive equation simulations? *Ocean Modelling, 39*(1), 183–199. https://doi.org/10.1016/j.ocemod.2010.09.007

Kamenkovich, I. V., & Pedlosky, J. (1996). Radiating instability of nonzonal ocean currents. *Journal of Physical Oceanography, 26*, 622–643. https://doi.org/10.1175/1520-0485(1996)026<0622:RIONOC>2.0.CO;2

Kamenkovich, I. V., & Pedlosky, J. (1998a). Radiation of energy from nonzonal ocean currents, nonlinear regime. Part I: Single wave development. *Journal of Physical Oceanography, 28*, 1661–1682. https://doi.org/10.1175/1520-0485(1998)028<1661:ROEFNO>2.0.CO;2

Kamenkovich, I. V., & Pedlosky, J. (1998b). Radiation of energy from nonzonal ocean currents, nonlinear regime. Part II: Interactions between waves. *Journal of Physical Oceanography, 28*, 1683–1701. https://doi.org/10.1175/1520-0485(1998)028<1683:ROEFNO>2.0.CO;2

Klinger, B. A., & Haine, T. W. N. (2019). *Ocean Circulation in Three Dimensions*. Cambridge University Press.

LaCasce, J. (2000). Floats and f/h. *Journal of Marine Research, 58*(1), 61–95. https://doi.org/10.1357/002224000321511205

LaCasce, J. H., Palóczy, A., & Trodahl, M. (2024). Vortices over bathymetry. *Journal of Fluid Mechanics, 979*, A32. https://doi.org/10.1017/jfm.2023.1084

Lorenz, E. N. (1955). Available potential energy and the maintenance of the general circulation. *Tellus, 7*(2), 157–167. https://doi.org/10.1111/j.2153-3490.1955.tb01148.x

Pedlosky, J. (1987). *Geophysical Fluid Dynamics*. Springer.

Pedlosky, J. (2003). *Waves in the Ocean and Atmosphere: Introduction to Wave Dynamics*. Springer.

Pegliasco C., Busché C., Faugère Y. Mesoscale eddy trajectory atlas META3.2 delayed-time all satellites: version META3.2 DT allsat. (2022). https://doi.org/10.24400/527896/A01-2022.005.210802.

Rayleigh, Lord. (1926). *The Theory of Sound* (Vol. 2). Macmillan.

Rhines, P. B. (1977). The dynamics of unsteady currents. In E. D. Goldberg, I. N. McCane, J. J. O'Brien, & J. H. Steele (Eds.), *The Sea* (Vol. 6, pp. 189–318). Wiley.

Robinson, A. R., & McWilliams, J. C. (1974). The baroclinic instability of the open ocean. *Journal of Physical Oceanography, 4*, 281–294. https://doi.org/10.1175/1520-0485(1974)004<0281:TBIOTO>2.0.CO;2

Salmon, R. (1998). *Lectures on Geophysical Fluid Dynamics*. Oxford University Press.

Sandalyuk, N. V., Belonenko, T. V., & Koldunov, A. V. (2021). Shelf Waves in the Great Australian Bight Based on Satellite Altimetry Data. *Izvestiya, Atmospheric and Oceanic Physics, 57*, 1117–1126. https://doi.org/10.1134/S0001433821090619

Smith, K. S. (2007). The geography of linear baroclinic instability in earth's oceans. *Journal of Marine Research, 65*(5), 655–683. https://doi.org/10.1357/002224007783649484

Spall, M. A. (2000). Generation of strong mesoscale eddies by weak ocean gyres. *Journal of Marine Research, 58*, 97–116. https://doi.org/10.1357/002224000321511214

Talley, L. D. (2011). *Descriptive Physical Oceanography: An Introduction* (6th ed.). Academic Press.

Talley, L. D. (1983). Radiating barotropic instability. *Journal of Physical Oceanography, 13*, 972–987. https://doi.org/10.1175/1520-0485(1983)013<0972:RBI>2.0.CO;2

Travkin, V. S., Gnevyshev, V. G., & Belonenko, T. V. (2024). Mesoscale eddies on the continental slope of the New Zealand Plateau based on altimetry data. *Sovremennye Problemy Distantsionnogo Zondirovaniya Zemli iz Kosmosa [Modern Problems of Remote Sensing of the Earth from Space], 21*(3), 221–233. https://doi.org/10.21046/2070-7401-2024-21-3-221-233

Travkin, V. S., & Belonenko, T. V. (2021). Study of the Mechanisms of Vortex Variability in the Lofoten Basin Based on Energy Analysis. *Physical Oceanography, 28*(3), 294–308. https://doi.org/10.22449/1573-160X-2021-3-294-308

Trodahl, M., & Isachsen, P. E. (2018). Topographic influence on baroclinic instability and the mesoscale eddy field in the northern North Atlantic Ocean and the Nordic Seas. *Journal of Physical Oceanography, 48*(11), 2593–2607. https://doi.org/10.1175/JPO-D-17-0220.1

Wang, J., Spall, M. A., Pedlosky, J., & Kamenkovich, I. (2019). Radiating instability and small-scale stochastic wind forcing. In B. Galperin & P. Read (Eds.), *Zonal Jets* (pp. 247–254). Cambridge University Press. https://doi.org/10.1017/9781107358225

Wang, J., Spall, M. A., Flierl, G. R., & Malanotte-Rizzoli, P. (2012). A new mechanism for the generation of quasi-zonal jets in the ocean. *Geophysical Research Letters, 39*(10), L10603. https://doi.org/10.1029/2012GL051861

Wang, J., Spall, M. A., Flierl, G. R., & Malanotte-Rizzoli, P. (2013). Nonlinear Radiating Instability of a Barotropic Eastern Boundary Current. *Journal of Physical Oceanography, 43*(7), 1439–1452. https://doi.org/10.1175/JPO-D-12-0174.1

Zatsepin, A. G., & Elkin, D. N. (2024). Underwater Ridge Impact on the Motion of Anticyclonic Eddies over a Sloping Bottom as a Result of the Topographic Beta-Effect: Laboratory Experiment. *Physical Oceanography, 31*(2), 271–283

Zhmur, V. V., Belonenko, T. V., Novoselova, E. V., et al. (2023a). Direct and Inverse Energy Cascades in the Ocean during Vortex Elongation. *Doklady Earth Sciences, 508*(2), 233–236. https://doi.org/10.1134/S1028334X22601675

Zhmur, V. V., Belonenko, T. V., Novoselova, E. V., et al. (2023b). On the stretching of mesoscale vortices into filaments and their distribution over the ocean surface. *Radiophysics and Quantum Electronics, 66*(2–3), 93–108. https://doi.org/10.1007/s11141-023-10278-4

Zhmur, V. V., Novoselova, E. V., & Belonenko, T. V. (2021). Potential Vorticity in the Ocean: Ertel and Rossby Approaches with Estimates for the Lofoten Vortex. *Izvestiya, Atmospheric and Oceanic Physics, 57*(6), 632–641. https://doi.org/10.1134/S0001433821050157

Zhmur, V. V., Travkin, V. S., Belonenko, T. V., et al. (2022). Transformation of Kinetic and Potential Energy during Elongation of a Mesoscale Vortex. *Physical Oceanography, 29*(5), 449–462. https://doi.org/10.22449/1573-160X-2022-5-449-462

Zhmur, V. V., Belonenko, T. V., Travkin, V. S., et al. (2023c). Changes in the Available Potential and Kinetic Energy of Mesoscale Vortices When They Are Stretched into Filaments. *Journal of Marine Science and Engineering, 11*(6), 1131. https://doi.org/10.3390/jmse11061131
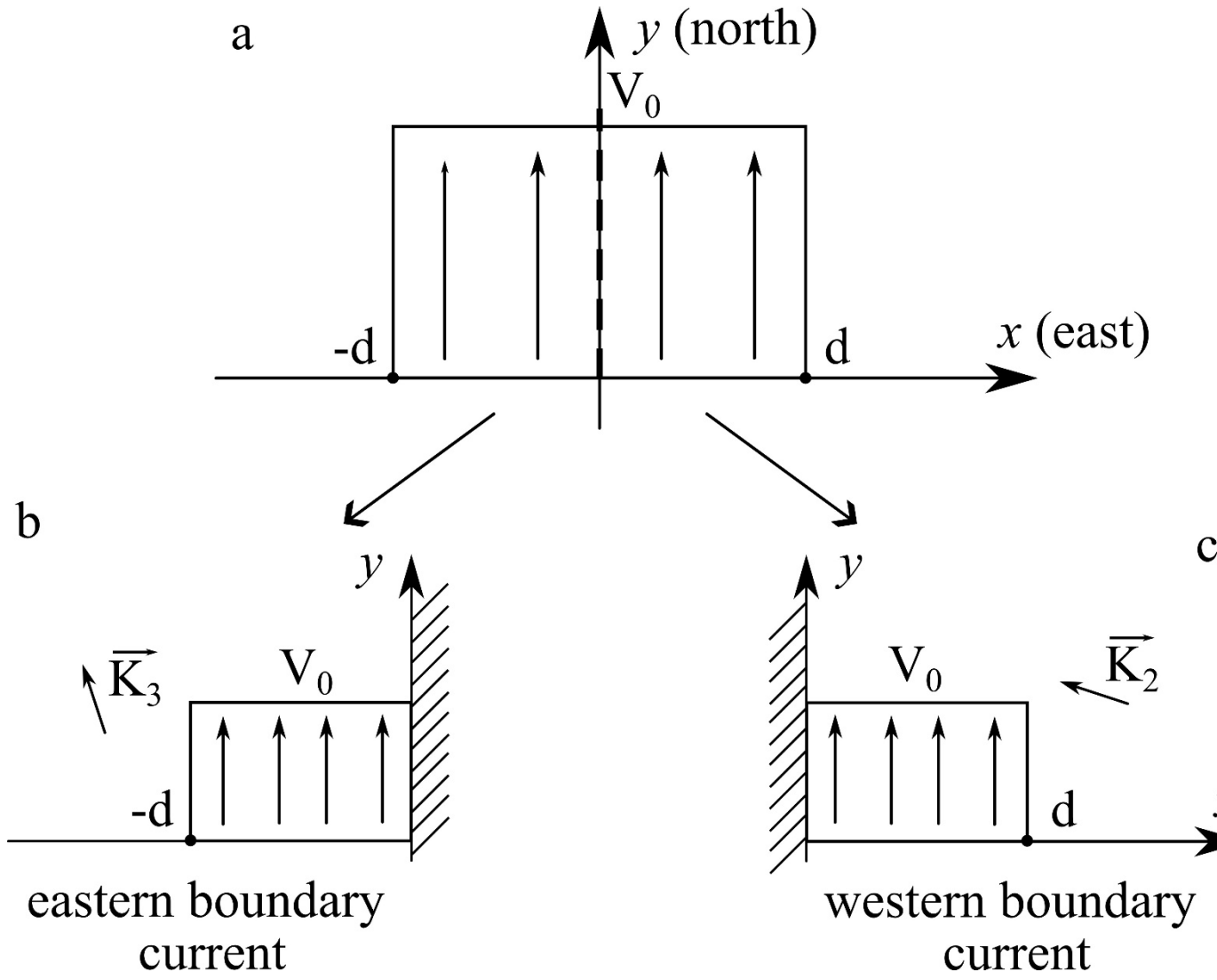
Fig. 1. Basic state for the stability problem. Configurations for a) rectangular flow; b) eastern boundary current; c) a western boundary current.
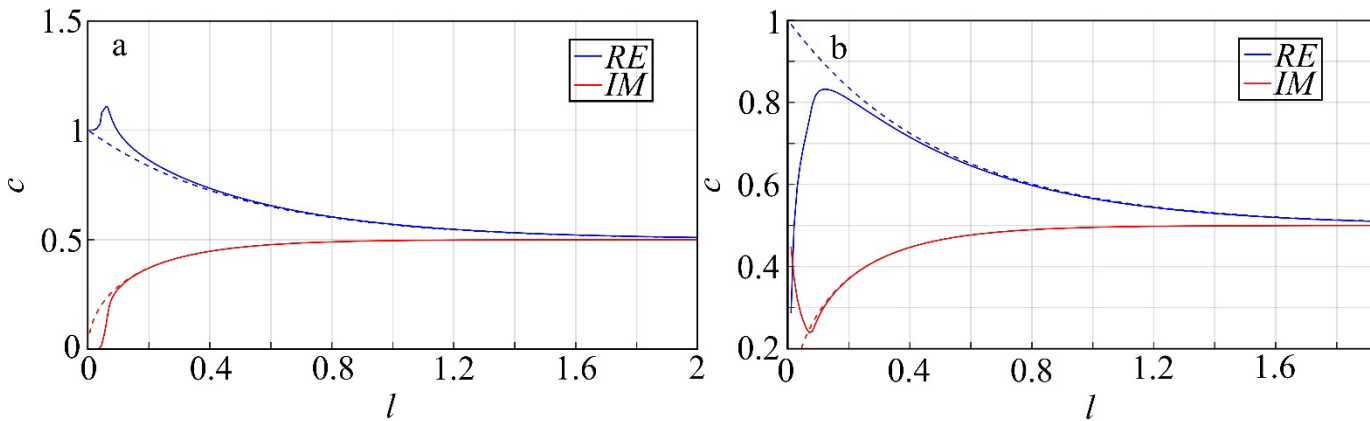

Fig. 2. Eigenvalues of phase velocity c as a function of l: a) for the western meridional boundary current at $\beta = 0.01$ (solid line); b) for the eastern meridional boundary current at $\beta = 0.01$ (solid line). Eigenvalues at $\beta = 0$ are shown by dashed lines.
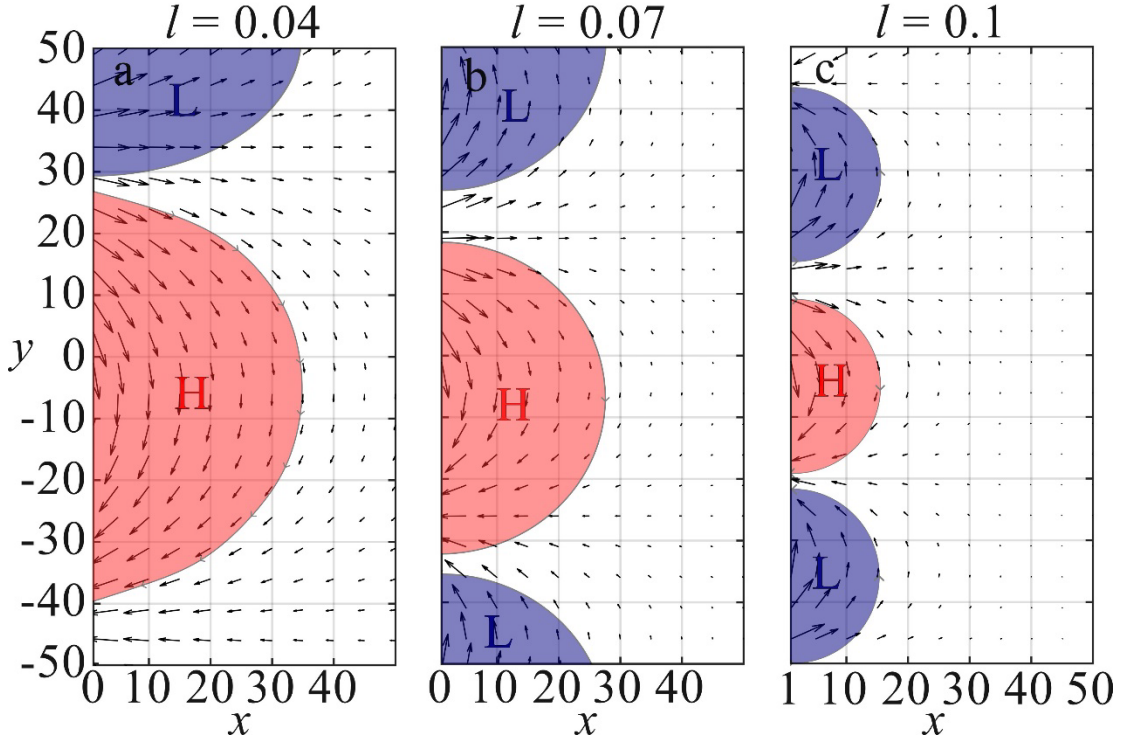
Fig. 3. The black vectors denote the surface absolute geostrophic velocity for the western boundary current at $\beta = 0$, $l = 0.04$ (a), 0.07 (b), and 0.1 (c). On the x and y axes are the spatial coordinates x and y of the Cartesian coordinate system, normalized to 100 km. The letters H and L denote areas of anticyclonic (H) and cyclonic (L) sea surface height, respectively.
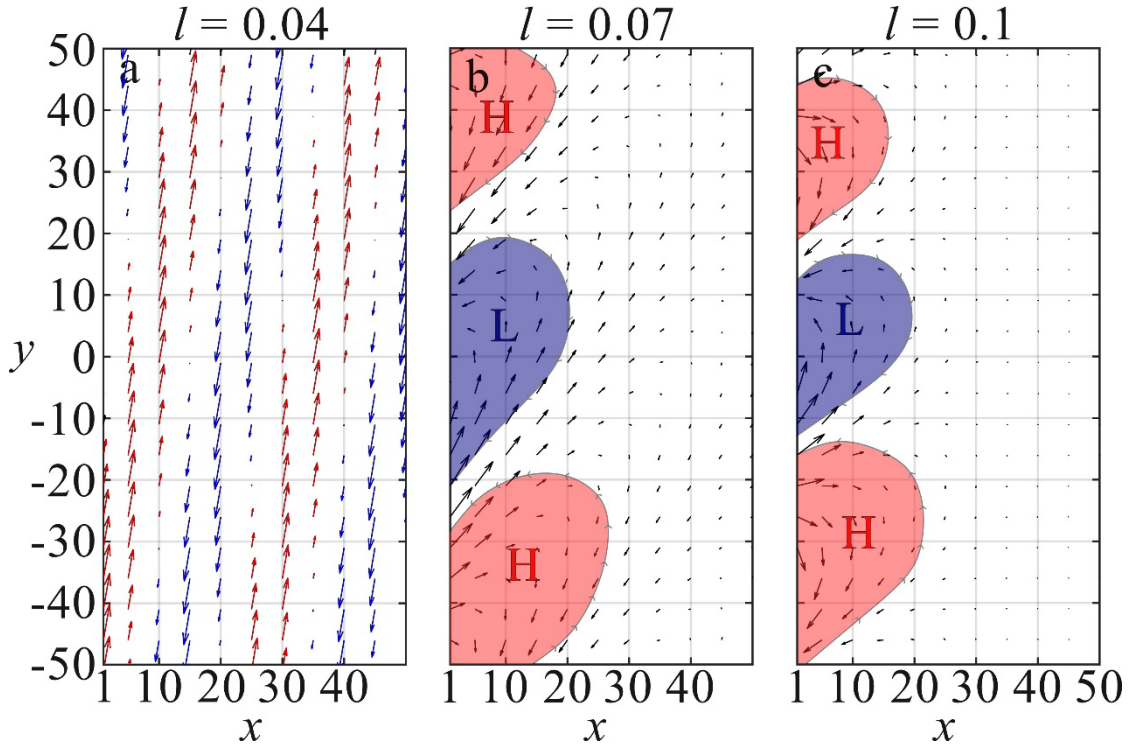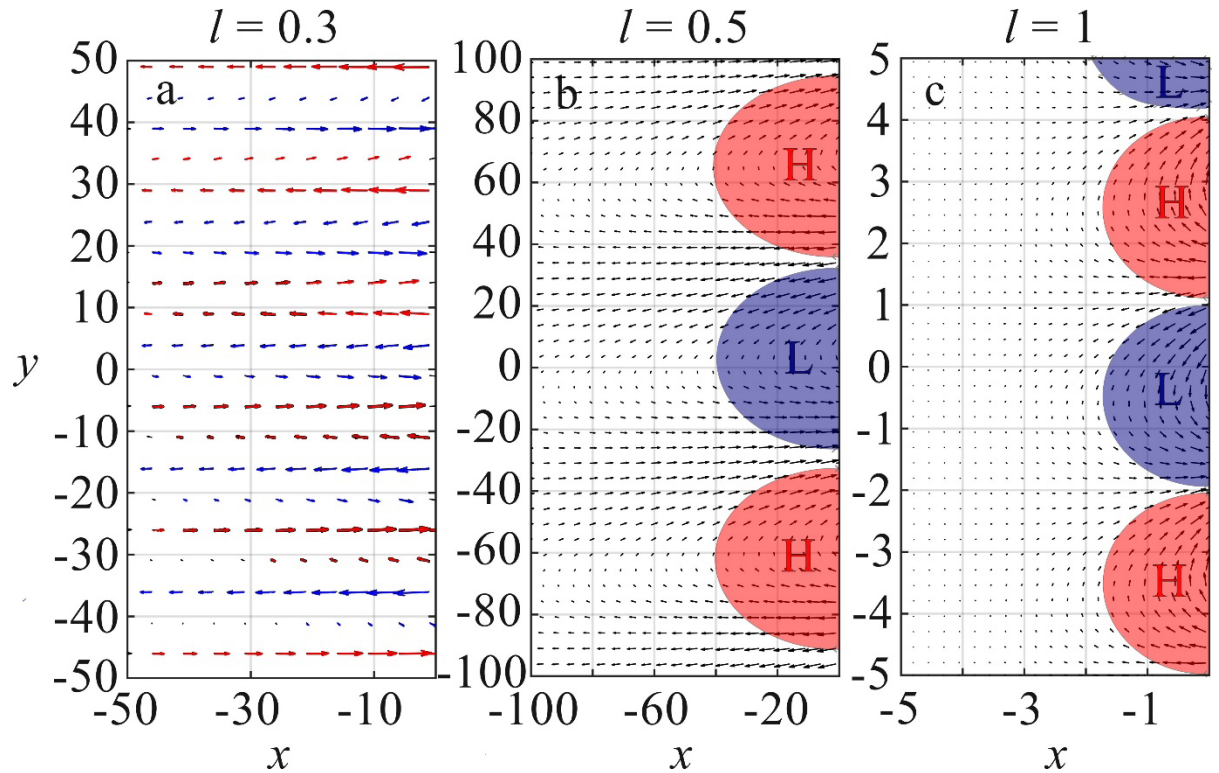

Fig. 4. Velocity values for the western boundary current at $\beta = 0.01$, $l = 0.04$ (a), 0.07 (b), and 0.1 (c). On the x and y axes are the spatial coordinates x and y of the Cartesian coordinate system, normalized to 100 km. The letters H and L denote areas of anticyclonic (H) and cyclonic (L) sea surface height, respectively.
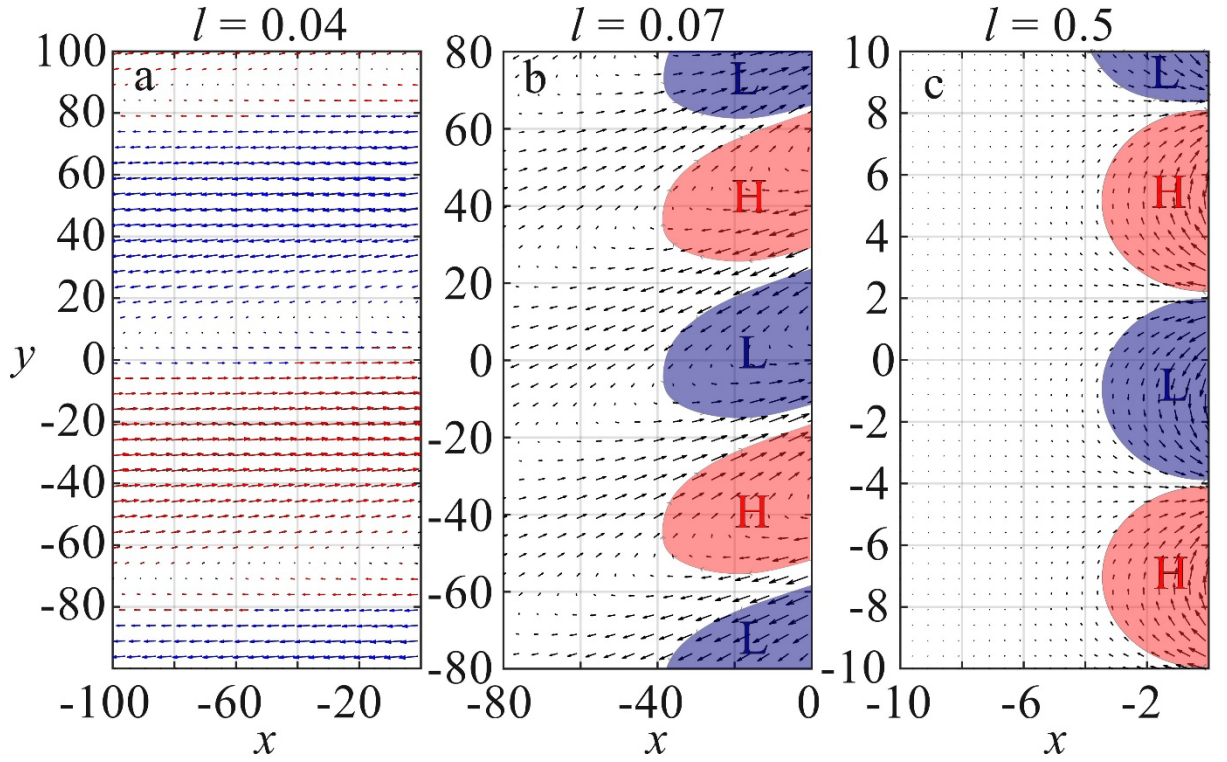
Fig. 5. Velocity values for the eastern boundary current at $\beta = 0.01$, $l = 0.04$ (a), $l = 0.07$ (b), and 0.5 (c). On the x and y axes are the spatial coordinates x and y of the Cartesian coordinate system, normalized to 100 km. The letters H and L denote areas of anticyclonic (H) and cyclonic (L) sea surface height, respectively.
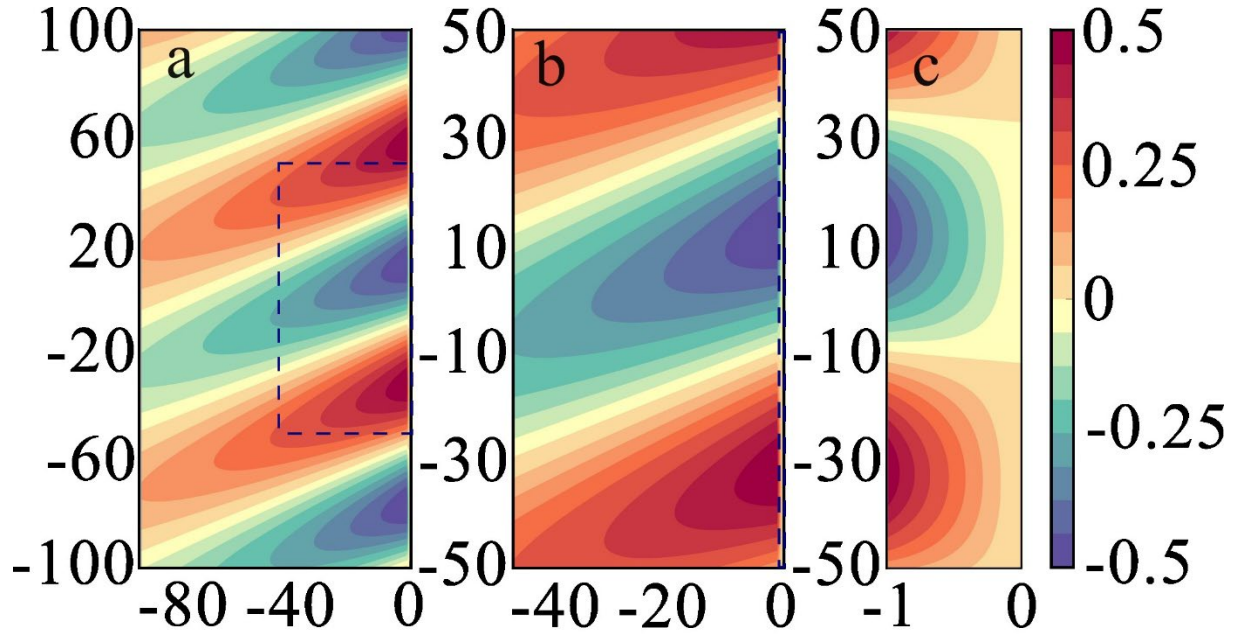
Fig. 6. Zonal displacement for the eastern boundary current at $\beta = 0.01$, $l = 0.07$ for various scales:a) $-100 \leq x \leq 0$, b) $-50 \leq x \leq 0$, and c) $-1 \leq x \leq 0$. On the x and y axes are the spatial coordinates x and y of the Cartesian coordinate system, normalized to 100 km. Colors show the values of η_1 and η_2, calculated using formulas (27). Blue dashed lines indicate individual parts of figure (a), shown in more detail (b and c).
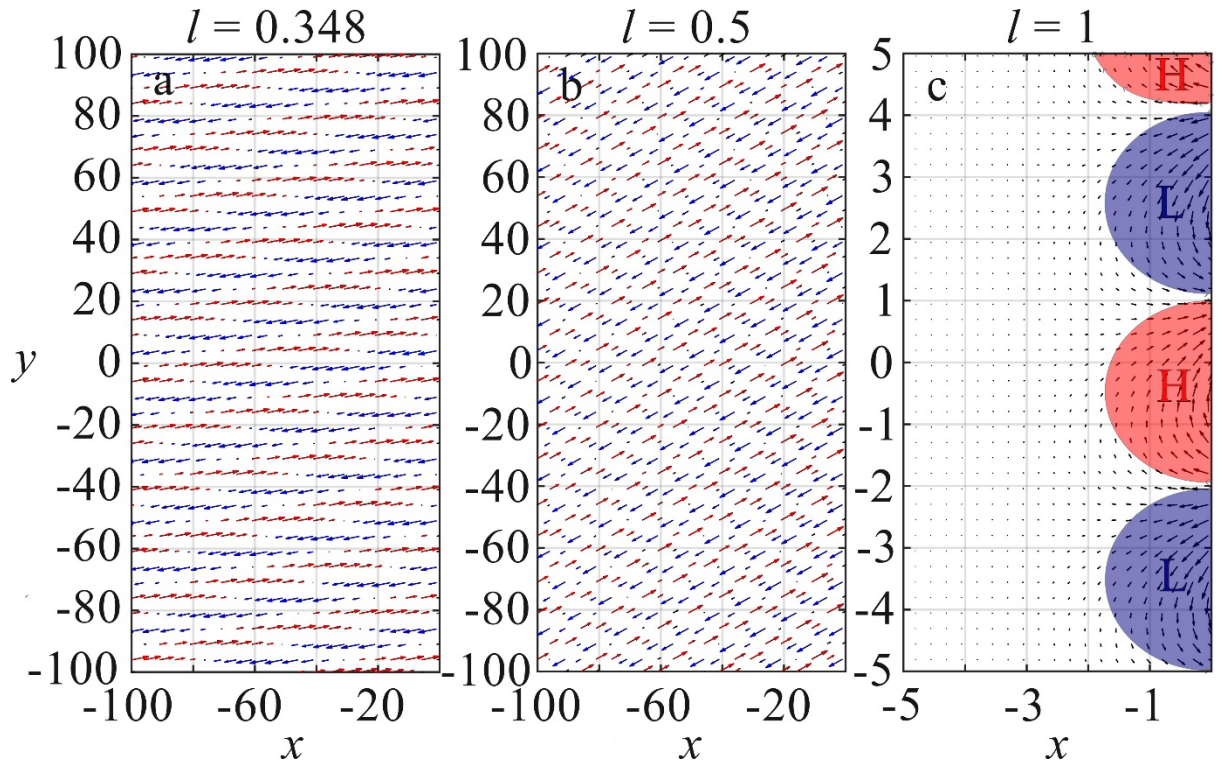
Fig. 7. Velocity values for the first mode of the eastern boundary current at $\beta = 0.5$, $l = 0.348$ (a), 0.5 (b), and 1 (c). On the x and y axes are the spatial coordinates x and y of the Cartesian coordinate system, normalized to 100 km. The letters H and L denote areas of anticyclonic (H) and cyclonic (L) sea surface height, respectively.


Fig. 8. Velocity values for the second mode of the eastern boundary current at $\beta = 0.5$, $l = 0.3$ (a), 0.5 (b), and 1 (c). On the x and y axes are the spatial coordinates x and y of the Cartesian coordinate system, normalized to 100 km. The letters H and L denote areas of anticyclonic (H) and cyclonic (L) sea surface height, respectively.
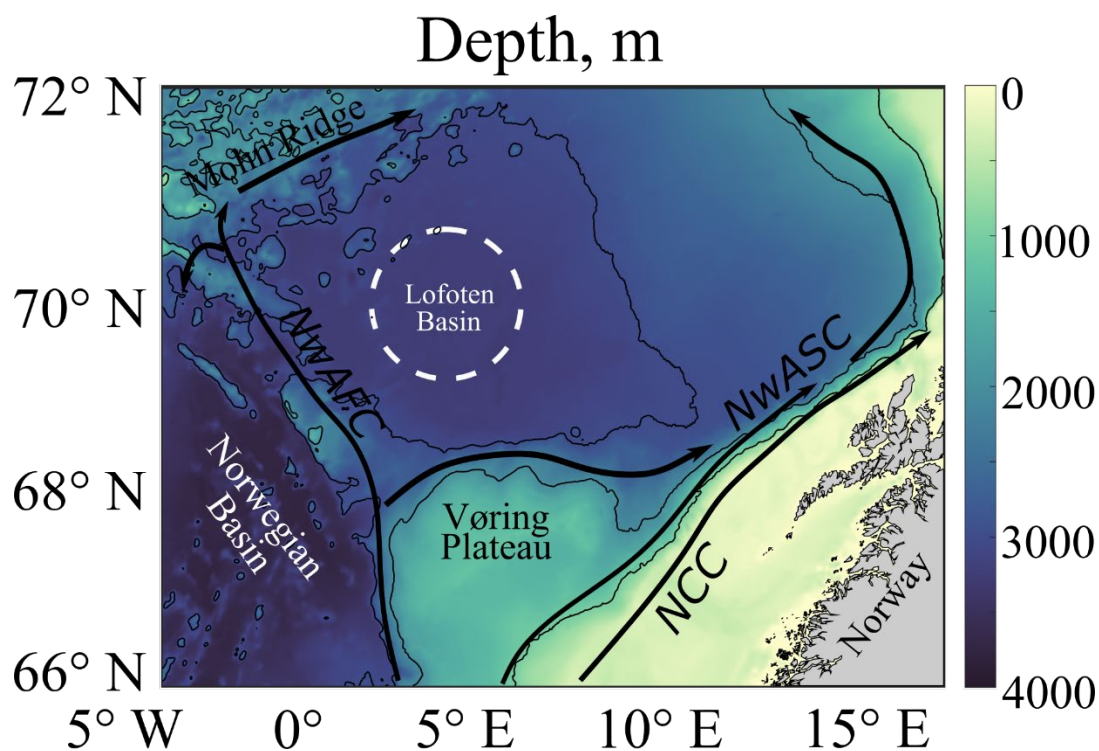
Fig. 9. Bottom topography (color) and general circulation (arrows) of the study region. The black lines indicate the main currents. Abbreviations: NCC – Norwegian Coastal Current, NwASC – Norwegian Atlantic Slope Current, NwAFC – Norwegian Atlantic Frontal Current.
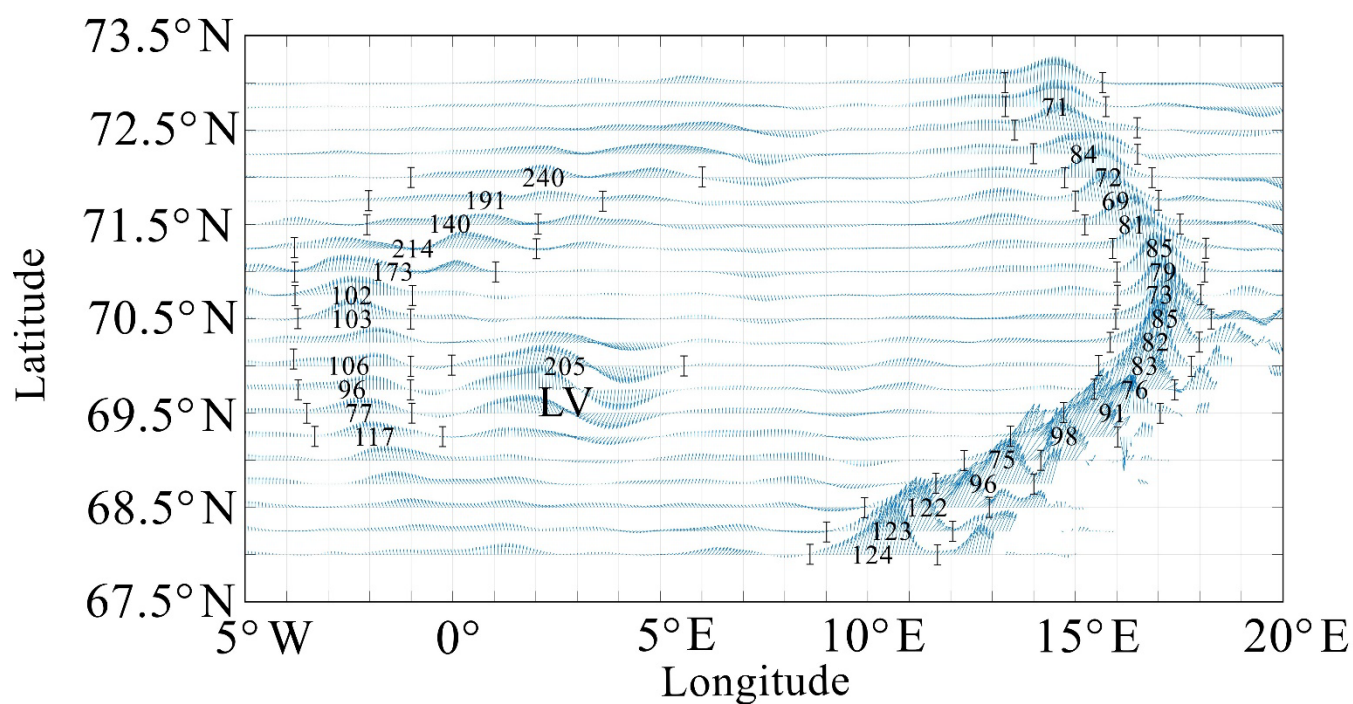
Fig. 10. Velocities and direction of surface currents in the Lofoten Basin, with numbers indicating jet width in km (between dashes). LV indicates the location of the Lofoten Vortex.
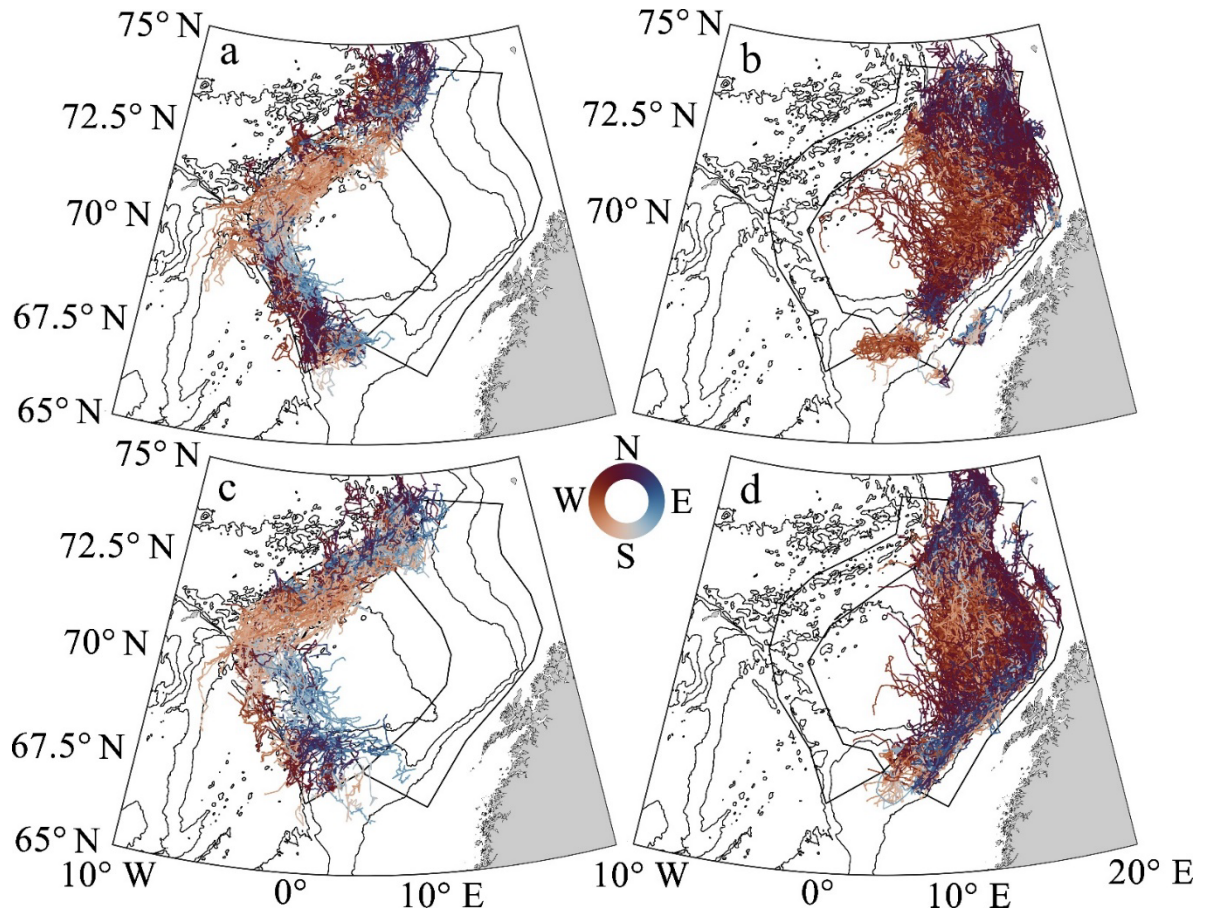
Fig. 11. Trajectories of mesoscale eddies – anticyclones (a, b) and cyclones (c, d) – formed on the western and eastern boundary currents. The direction of eddy movement is indicated by color, masks are shown in black. Isobaths are drawn at 1000 m intervals.